



## Rain-induced turbulence and air-sea gas transfer

Christopher J. Zappa,<sup>1</sup> David T. Ho,<sup>1,2</sup> Wade R. McGillis,<sup>1,3</sup> Michael L. Banner,<sup>1</sup> John W. H. Dacey,<sup>4</sup> Larry F. Bliven,<sup>5</sup> Barry Ma,<sup>6,7</sup> and Jeff Nystuen<sup>6</sup>

Received 2 July 2008; revised 18 March 2009; accepted 21 April 2009; published 9 July 2009.

[1] Results from a rain and gas exchange experiment (Bio2 RainX III) at the Biosphere 2 Center demonstrate that turbulence controls the enhancement of the air-sea gas transfer rate (or velocity)  $k$  during rainfall, even though profiles of the turbulent dissipation rate  $\varepsilon$  are strongly influenced by near-surface stratification. The gas transfer rate scales with  $\varepsilon^{1/4}$  for a range of rain rates with broad drop size distributions. The hydrodynamic measurements elucidate the mechanisms responsible for the rain-enhanced  $k$  results using SF<sub>6</sub> tracer evasion and active controlled flux technique. High-resolution  $k$  and turbulence results highlight the causal relationship between rainfall, turbulence, stratification, and air-sea gas exchange. Profiles of  $\varepsilon$  beneath the air-sea interface during rainfall, measured for the first time during a gas exchange experiment, yielded discrete values as high as  $10^{-2}$  W kg<sup>-1</sup>. Stratification modifies and traps the turbulence near the surface, affecting the enhancement of the transfer velocity and also diminishing the vertical mixing of mass transported to the air-water interface. Although the kinetic energy flux is an integral measure of the turbulent input to the system during rain events,  $\varepsilon$  is the most robust response to all the modifications and transformations to the turbulent state that follows. The Craig-Banner turbulence model, modified for rain instead of breaking wave turbulence, successfully predicts the near-surface dissipation profile at the onset of the rain event before stratification plays a dominant role. This result is important for predictive modeling of  $k$  as it allows inferring the surface value of  $\varepsilon$  fundamental to gas transfer.

**Citation:** Zappa, C. J., D. T. Ho, W. R. McGillis, M. L. Banner, J. W. H. Dacey, L. F. Bliven, B. Ma, and J. Nystuen (2009), Rain-induced turbulence and air-sea gas transfer, *J. Geophys. Res.*, *114*, C07009, doi:10.1029/2008JC005008.

### 1. Introduction

[2] Atmosphere-ocean interactions play a crucial role in the regional and global budgets of biogeochemical trace gases and in the transport of volatile pollutants. A plethora of processes has been shown in individual studies to play varying roles in regulating air-sea gas fluxes, which continually work to adjust the balance of constituents in the upper ocean. Therefore, a better understanding of mechanisms controlling air-water gas exchange and ocean mixing is needed to improve model predictions of the spatial variability of air-sea fluxes.

[3] The flux,  $F$ , of a sparingly soluble gas can be parameterized as the product of the chemical potential gradient of the gas between the air and water, and the gas transfer velocity,  $k$ , which embodies the details of the turbulence-mediated transfer across the surface aqueous mass boundary layer (MBL). The chemical potential gradient of the gas can be defined involving a variety of expressions of solubility. The solubility of a gas also prescribes whether a gas is either liquid-phase or gas-phase controlled [Liss and Slater, 1974] and is also important in bubble-mediated processes [Asher and Wanninkhof, 1998; Keeling, 1993; Merlivat and Memery, 1983; Woolf, 1993]. Near-surface turbulence is presumed to be the driving mechanism that regulates  $k$  across the air-water interface in the absence of bubbles. The magnitude of  $k$  is determined by the molecular diffusivity of a gas and the spatially and temporally varying MBL, whose thickness is a function of near surface turbulence and diffusivity.

[4] Wind has long been known to drive gas exchange in the open ocean because it plays a central role in the generation of turbulence through the transfer of momentum to waves and currents. As a result, numerous relationships between  $k$  and wind speed have been developed [e.g., Ho et al., 2006; Liss and Merlivat, 1986; Nightingale et al., 2000; Wanninkhof, 1992; Wanninkhof and McGillis, 1999]. However, many processes and mechanisms, both related and unrelated to wind-forcing, have been determined to influence gas exchange, including short wind waves [e.g., Bock et al., 1999; Jähne

<sup>1</sup>Lamont-Doherty Earth Observatory, Earth Institute at Columbia University, Palisades, New York, USA.

<sup>2</sup>Now at Department of Oceanography, University of Hawai'i at Manoa, Honolulu, Hawaii, USA.

<sup>3</sup>Department of Earth and Environmental Engineering, Columbia University, New York, New York, USA.

<sup>4</sup>Biology Department, Woods Hole Oceanographic Institution, Woods Hole, Massachusetts, USA.

<sup>5</sup>Laboratory for Hydrospheric Processes, NASA Goddard Space Flight Center, Wallops Island, Virginia, USA.

<sup>6</sup>Applied Physics Laboratory, University of Washington, Seattle, Washington, USA.

<sup>7</sup>Now at Electrical and Computer Engineering, Portland State University, Portland, Oregon, USA.

*et al.*, 1987], microscale wave breaking [Zappa *et al.*, 2001, 2004], bubble-mediated transfer [Asher and Wanninkhof, 1998; Farmer *et al.*, 1993; Woolf and Thorpe, 1991; Woolf, 1993], organic films [Frew, 1997; Frew *et al.*, 2004], and rain [Ho *et al.*, 1997, 2000]. Regardless of the specific processes and the details of the underlying physics, models generally attempt to parameterize  $k$  on the basis of the assumption that turbulence regulates the exchange in the absence of bubbles.

[5] The turbulence-mediated transfer across the MBL has been explicitly related to the turbulent kinetic energy (TKE) dissipation rate,  $\varepsilon$ . The resulting physical scaling relationship for gas transfer is

$$k \propto (\varepsilon\nu)^{1/4} Sc^{-n}, \quad (1)$$

where the Schmidt number,  $Sc$ , is defined as the ratio of the kinematic viscosity of water,  $\nu$ , to mass diffusivity  $D$ , and  $Sc$  exponent  $n$  varies between 1/2 (clean surface) and 2/3 (highly contaminated surface or rigid wall) depending on the surface boundary conditions [Jähne *et al.*, 1987; Ledwell, 1984]. This relationship is consistent with mass diffusion across a layer of the thickness of the Batchelor [1959] scale  $\delta_B = Sc^{-1/2}\eta$ , where  $\eta = (\nu^3/\varepsilon)^{1/4}$  is the Kolmogorov, or dissipative, microscale [Melville, 1996]. This expression has been derived by Kitaigorodskii [1984] in the context of modeling the influence of patches of enhanced turbulence by breaking. A similar scaling was developed for modeling the mass transfer of falling wavy turbulent liquid films [Banerjee *et al.*, 1968], and has also been derived using surface renewal theory [Lamont and Scott, 1970]. This scaling demonstrates that increasing turbulence will enhance  $k$ , and this scaling has been tested with success in laboratory grid-mixing tanks for varying surface conditions [Asher and Pankow, 1986; Dickey *et al.*, 1984]. Recently, this scaling has been shown to work in a variety of environmental systems and forcings [Zappa *et al.*, 2007] and has been suggested as a unified relationship for interfacial fluxes at both the benthic and air-sea boundary layers [Lorke and Peeters, 2006].

[6] Raindrops falling on a freshwater surface have been shown to enhance  $k$  in laboratory experiments and preliminary field studies. These studies showed that the rain-induced gas exchange increased with the kinetic energy flux (KEF) applied to the water surface by the raindrops [Ho *et al.*, 1997, 2000]. Ho *et al.* [2000] inferred that the enhancement in  $k$  by rain is dominated by the production of turbulence from the KEF of the raindrops, whereas rain-generated bubbles contribute 0–20% of the total gas exchange. However, the bulk KEF relationship was developed on the basis of experiments that were not representative of rain conditions found in nature because they used raindrops of discrete size. This result opens the door for quantifying the gas transfer rate on the basis of the physical relationship in (1).

[7] During a previous rain and gas exchange experiment at the Biosphere 2 ocean (Bio2 RainX II), an SF<sub>6</sub> tracer release experiment was performed to quantify rain-induced gas exchange in saltwater conditions [Ho *et al.*, 2004]. The measurements show the rapid depletion of SF<sub>6</sub> in the near-surface layer due to rain enhancement of gas exchange, and the gas transfer velocity was similar to that in freshwater experiments. However, Ho *et al.* [2004] suggested that the near-

surface layer was not replenished as fast as it was depleted because rainfall in a saltwater body promotes density stratification of the upper water column that inhibits vertical mixing of higher-concentration SF<sub>6</sub> from below. Therefore, the overall gas flux was lower than that found during freshwater experiments. In addition to the SF<sub>6</sub> evasion measurements, direct velocity measurements in the bulk water showed an increase in the turbulent dissipation rate,  $\varepsilon$ , during the rain events. This increase in  $\varepsilon$  supports a link between turbulence and enhanced gas transfer in the presence of rain. However, the turbulent dissipation was measured at a fixed-point 30 cm from the surface aqueous boundary layer and the dynamics of the generation of the turbulence profile in the presence of stratification were unclear. Measurements of Green and Houk [1979] and Lange *et al.* [2000] suggest that turbulent mixing due to rainfall penetrates down to  $O(10)$ cm. Rain-induced density stratification may affect the turbulence in the surface aqueous boundary layer and the ability to predict  $k$ . Thus, the behavior and properties of these processes need to be understood and measured for development of adequate models for rain-induced gas exchange.

[8] In the following, results of a follow-up experiment conducted at the Biosphere 2 ocean, Bio2 RainX III, are presented. The gas transfer velocity was determined by performing an SF<sub>6</sub> evasion experiment, as well as by implementing the active controlled flux technique (ACFT) [Zappa *et al.*, 2004]. Raindrop size distributions and rain rates were measured with a Rain Imaging System (RIS) and a Passive Acoustic Listener (PAL). Rain rates were also determined with a pressure transducer and with buckets. Turbulence profiles were measured with an acoustic DopBeam that also measured the surface wavefield and rain rate. Records of high-resolution temperature and salinity gradients were made using a profiling CTD (Seabird SBE-37), and the thermal signature of water surface was measured using an infrared (IR) imager. Together, these measurements allow the study of the influence of rain on air-sea gas exchange, as well as to elucidate the mechanisms responsible for the observed effect.

## 2. Methods

[9] During Bio2 RainX III, four rain experiments were conducted. The first (RE1) was a long rain event (175 min) with a moderate rain rate. The second (RE2) was a short rain event (16 min) in an attempt to attain the maximum rain rate of the facility. The third (RE3) was another short event (24 min) at a moderate rain rate. The final (RE4) was a long rain event (134 min). The lengths of these rain events were dictated by the fresh water storage capacity of the reservoirs, by the range of tolerable water level in the Biosphere 2 ocean, as well as the salinity limit imposed by the requirements of organisms in the ocean.

### 2.1. Biosphere 2 Ocean

[10] The Biosphere 2 ocean is ideally suited to conduct controlled experiments on rain-induced air-sea gas exchange and its utility has been well documented by Ho *et al.* [2004]. The Biosphere 2 ocean contains 2,650 m<sup>3</sup> of saltwater with a nominal salinity of 35.5. The ocean has a surface area of approximately 675 m<sup>2</sup> and much of the deep ocean is greater

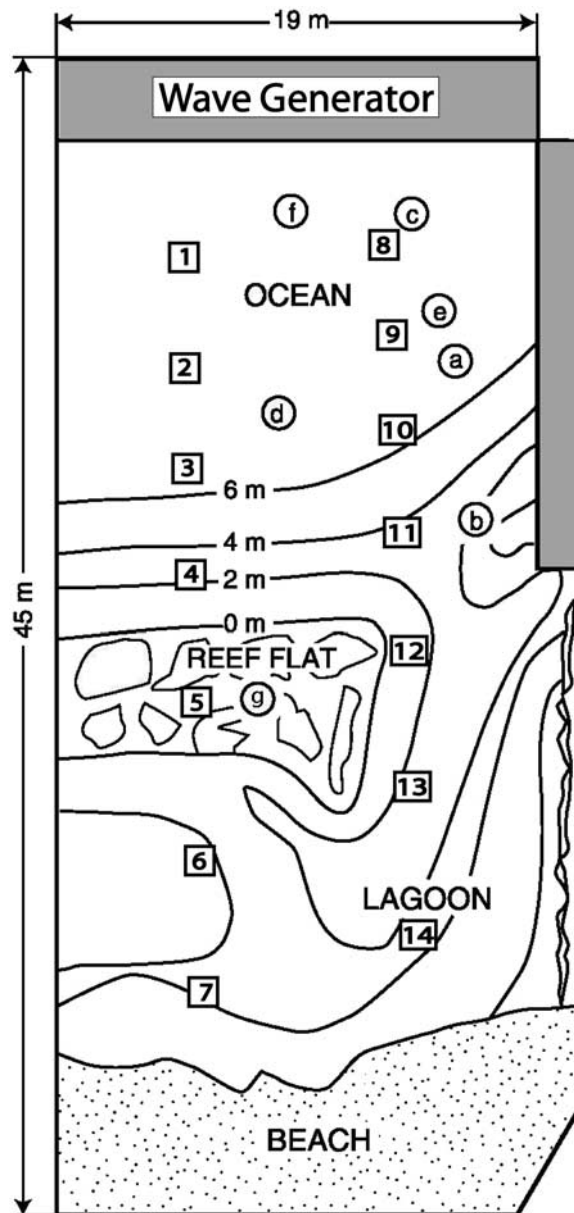


**Figure 1.** The Biosphere 2 ocean: 45-m long, 19-m wide, with depth of the bottom varying from about 0.5 to 7 m. Indicated (as circled letters) are the locations of various instruments during Bio2 RainX III: a, SF<sub>6</sub> and salinity sampler; b, pulse-to-pulse coherent Doppler sonar system (DopBeam) and Modular Acoustic Current System (MAVS); c, bottom-mounted YSI (temperature, pressure); d, autonomous Seabird Microcat CTD Profiler; e, area measured by infrared IR imager and used for active controlled flux technique (ACFT); f, PAL; and g, Rain Imaging System (RIS). Also indicated are the 14 locations (numbered in square boxes) for the 10-cm buckets in Table 2.

than 6-m depth with a shelf reef that links the deep ocean at one end to a semi-enclosed lagoon at the other (see Figure 1). The ocean was maintained at a constant temperature of 26.5°C by pumps that circulate the ocean water through a heat exchanger during all rain events except RE1. At the deep

end of the ocean, a vacuum wave generator along the entire length of the wall creates energetic waves that propagate toward the lagoon, circulate water in the ocean, and generate ambient turbulence to promote air-water gas exchange. For a more detailed description of the Biosphere 2 ocean, see *Atkinson et al.* [1999] and *Ho et al.* [2004].

[11] The rain generation system is supplied from two water reservoirs (36 and 57 m<sup>3</sup>) using groundwater that had been purified by reverse osmosis. The system used for generating rain during Bio2 RainX III consisted of a series of nine PVC pipes strung across the ocean. Descending from each pipe were 3 rain heads, for a total of 27 rain heads. The rain heads were commercially available irrigation devices modified with short pieces of latex tubing that were oriented facing up (head inverted). Previous measurements show that the flexible tubing encouraged random dispersion of the drops, as well as a spectrum of drop sizes that was not too different than natural raindrop size distribution [*Ho et al.*, 2004]. The rain heads were located 10 m above the ocean, allowing raindrops to approach terminal velocity before impacting the surface. The nine lines of the rain generation system can be turned on and off independently depending on the desired rain rate. Not using all 9 lines may result in spatial variability in the rain rate. During RE1, lines 1, 3, 5, 7, and 9 were used. During RE2, all 9 lines were used. During RE3 and RE4, lines 2, 4, 6, and 8 were used. Regardless of which lines were used, the whole water surface including the ocean, the reef flat, and the lagoon, was agitated by rain.

## 2.2. SF<sub>6</sub> Evasion Experiment

[12] An SF<sub>6</sub> evasion experiment was conducted during RE4 to obtain an integrated measurement of gas transfer velocity. The experimental methods and procedures were nearly identical to those used during Bio2 RainX II, and described in detail by *Ho et al.* [2004]. About 12 h before RE4, a predetermined amount of SF<sub>6</sub> dissolved in water ( $\sim 1.3 \times 10^{-5}$  moles) was injected into the ocean using a 60 ml syringe. During RE4, samples for SF<sub>6</sub> and salinity measurements were drawn from 14 different depths in the ocean (1, 2, 3, 5, 8, 17, 34, 55, 75, 96, 141, 220, 410, and 500 cm) every 20 min using a sample profiler [*Ho et al.*, 2004]. Sampling for SF<sub>6</sub> and salinity continued for 24 h after RE4.

[13] Water used to generate rain at Biosphere 2 during RainX III contained a discernable amount of SF<sub>6</sub> from unknown sources. A correction was applied to the measured SF<sub>6</sub> concentration  $C_m(z)$  to deconvolve the decrease in SF<sub>6</sub> in the ocean due to gas exchange from the increase in SF<sub>6</sub> due to addition by rainwater and obtain a the corrected SF<sub>6</sub> concentration  $C(z)$ :

$$C(z) = C_m(z) \left( \frac{s_0}{s(z)} \right) - C_r \left( \frac{s_0 - s(z)}{s(z)} \right), \quad (2)$$

where  $s_0$  is the pre-rain ocean salinity,  $s(z)$  is the salinity measured concurrently with  $C_m(z)$ , and  $C_r$  is the measured SF<sub>6</sub> concentration of the rainwater. The mean SF<sub>6</sub> concentration in the ocean and the gas transfer velocity were then determined using methods described by *Ho et al.* [2004] (equations (2) to (6)).

[14] The gas transfer velocity for SF<sub>6</sub> was normalized to a Schmidt number ( $Sc$ ) of 600, corresponding to values for CO<sub>2</sub> at 20°C using the relationship:

$$k(600) = k_{SF_6} \left( \frac{600}{Sc_{SF_6}} \right)^{-n}, \quad (3)$$

where  $k_{SF_6}$  and  $Sc_{SF_6}$  are the gas transfer velocity and the Schmidt number for SF<sub>6</sub> (828 for our experiment), respectively. It has been shown in models and experiments that for a clean wavy water surface, in the absence of bubbles,  $n$  equals 1/2 [Brumley and Jirka, 1988; Jähne et al., 1987; Ledwell, 1984].

### 2.3. Rain Rate and Drop Size Distribution

[15] The raindrop size distribution (DSD) was obtained using the Rain Imaging System (RIS) developed at NASA and described in detail by Ho et al. [2004]. The RIS is an optical system consisting of an analog black and white video camera that is pointed at a halogen flood lamp. The RIS camera and light were located on the coral reef (see Figure 1).

[16] Ho et al. [1997] proposed and subsequent studies have shown [Ho et al., 2000, 2004] that rain-induced air-water gas exchange is correlated to rain kinetic energy flux (KEF). Recently, Takagaki and Komori [2007] proposed that the momentum flux of the raindrops (MF) is the more relevant scaling parameter. The KEF and MF are defined as

$$KEF = \frac{1}{2} \rho V v^2 n_d = \frac{1}{2} \rho R v^2 \quad (4a)$$

$$MF = \rho V v n_d = \rho R v \quad (4b)$$

where  $\rho$  is the density of water,  $V$  is the volume of a raindrop,  $R$  is the rain rate,  $n_d$  is the number of raindrops, and  $v$  is the velocity of the raindrop in cm s<sup>-1</sup>.

[17] Takagaki and Komori [2007] suggest that their gas transfer velocities were well parameterized by MF, but not with KEF. However, their data show only slightly better agreement with an MF scaling at low MF and KEF but also show slightly better agreement with a KEF scaling at higher MF and KEF. Their results actually show no statistically significant difference between a correlation of  $k$  with MF or KEF. Furthermore, comparisons with the previous rain and gas exchange studies show that both KEF and MF collapse the data similarly and no difference can be concluded. This suggests that KEF is nearly equivalent to MF for the parameterization of rain-induced gas transfer.

[18] Our current data set will not provide a conclusive answer to the KEF or MF debate. However, the raindrop size distributions and raindrop terminal velocities described here are comparable to those found in nature. The purpose of our study is to explore the effect of turbulence (TKE dissipation rate) and stratification on the rain-induced gas exchange including the implementation of a turbulence closure model that is intrinsically based on energy arguments. Therefore, we have chosen to present KEF for the purpose of our present work and for consistency with our previous studies.

[19] KEF can be derived from a DSD according to:

$$KEF = \frac{\rho}{2} \frac{\pi}{6} 10^{-6} \int v^3 D^3 N dD \quad (5)$$

where  $N$  is the raindrop size distribution,  $D$  is drop diameter in cm,  $v$  is the velocity of the raindrop in cm s<sup>-1</sup>, and KEF has units J m<sup>-2</sup> s<sup>-1</sup>. At Biosphere 2, the 10 m height was sufficient for drops to approach terminal velocity. Thus, a relationship of Lhermitte [1988] was used as a realistic estimate of drop terminal velocities  $v$  in the RIS measurement volume:

$$v(D) = v_o (1 - \exp[-(6.8D^2 + 4.88D)]) \quad (6)$$

where  $v_o$  is 923 cm s<sup>-1</sup> assuming that the measurement is performed at ground level.

[20] We also deployed a Passive Aquatic Listener (PAL) to quantify rain rate and drop size distribution during Bio2 RainX III. The PAL consists of an ITC-8263 hydrophone, signal pre-amplifiers and a recording computer (Tattletale-8). Details on the instrument description and application are given by Ma and Nystuen [2005]. The nominal sensitivity of these instruments is -160 dB relative to 1 V  $\mu$ Pa<sup>-1</sup> and the equivalent oceanic background noise level of the pre-amplifier system is about 28 dB relative to 1  $\mu$ Pa<sup>2</sup> Hz<sup>-1</sup>. A data collection sequence consists of four 1024 point time series collected at 100 kHz (10.24 ms each) separated by 5 s if triggered by rain or drizzle. Each time series is fast Fourier transformed (FFT) to obtain a 512-point (0–50 kHz) power spectrum. These four spectra are averaged together and spectrally compressed to 64 frequency bins, with frequency resolution of 200 Hz from 100 to 3,000 Hz and 1 kHz from 3 to 50 kHz. These spectra are evaluated individually to detect the acoustic signature of rainfall and then are recorded internally. The drop size distribution is then calculated by an acoustic inversion technique described by Nystuen [2001].

[21] The spatial distribution of the simulated rain was assessed using water volume measurements from twelve 10-cm diameter buckets. The buckets sat on floats, which were each tethered by a 1-m line to one of two ropes that extended from the wave generator to the beach. A YSI pressure and temperature sensor was deployed on the bottom of the deep part of the ocean (see Figure 1). The pressure sensor was used to estimate the bulk rain rate for the whole reservoir by taking the increase in depth over time.

### 2.4. High-Resolution Temperature and Salinity Profiles

[22] The evolution of a freshwater lens both during and after the rain events was important to quantify during Bio2 RainX III. High-resolution vertical profiles of salinity and temperature were measured using a Seabird Microcat Model SBE 37-SIP raised and lowered on an automated pulley system. The pulley was suspended from the ceiling above the ocean and a DC motorized winch was used to control the sensor depth in the water. During the experiment, the Microcat was deployed at the deep end of the ocean (6.5 m), adjacent to the wave generator (Figure 1). To minimize wake contamination from instrument and wire perturbation, only the upward profiles were used since the instrument sensors were facing upward. The Seabird Microcat sensor was set to report data at 1-s intervals, and was raised and lowered at

4.81 cm s<sup>-1</sup>. Data output from the sensor was used to regulate the vertical excursion of the sensor by stopping the motion when the detector reached the water surface on the upward motion and 4.5-m depth on the downward motion. Profiles were made every 3 min, starting at depth, rising to the surface, pausing, and then returning to depth.

## 2.5. Turbulence and Wave Measurements

[23] Measurements of velocity were made using a coherent Doppler sonar. The DopBeam (Sontek) is a 1.5-MHz monostatic, single-beam sonar system performing pulse-to-pulse coherent Doppler measurements of the along-beam fluid velocity. Details on the DopBeam operation and implementation are given by *Zedel et al.* [1996] and *Veron and Melville* [1999]. For our configuration, the DopBeam measured velocities at a repetition rate of 375 Hz along the beam in 125 bins 1.2 cm width each. During the pulse-pair processing, the velocity is determined by taking the time rate of change of the phase of the complex signal autocorrelation and is averaged down to 10 Hz. A “dead” zone exists within 15 cm of the 2.5-cm diameter transducer where the DopBeam is not able to measure velocity because of the delay between transmitting and receiving the acoustic signal. The cutoff for the correlation coefficient is given as 0.85 below which is defined as bad data from the DopBeam.

[24] A second velocity measurement was provided by a modular acoustic velocity sensor (MAVS; Nobska) by measuring the differential travel time of an acoustic pulse between a transmitter and receiver. The MAVS provided a measurement of  $x$ ,  $y$ , and  $z$  axis velocity components ( $u$ ,  $v$ , and  $w$ , respectively). Mean flow velocity and turbulent velocity (dissipation rate) statistics were estimated from 10 min records sampled at 22 Hz. The mean current is calculated as  $V = (\bar{u}^2 + \bar{v}^2)^{1/2}$  where overbars denote 10 min averages.

[25] The DopBeam was rigidly boomed out horizontally from the dock such that the acoustic transducer/receiver head of the instrument was 3 m from the dock at an initial depth of 0.7 m and directed toward the ocean surface (see Figure 1). The MAVS Instrument was mounted similarly such that the sensing volume was at a depth of 0.5 m and 0.75 m adjacent to the DopBeam. The locations of the DopBeam and MAVS during Bio2 RainX III are shown in Figure 1. In this configuration, the DopBeam provides a profile of vertical velocity near the ocean surface and the MAVS provides continuous 3-component velocity at depth.

[26] In steady flow with isotropic, fully developed turbulence, kinetic energy is transferred from the mean flow to large eddies, then on to smaller eddies, and is finally dissipated by viscosity. Under these conditions, the turbulent dissipation rate,  $\epsilon$ , can be estimated by the magnitude of the wave number spectrum in the inertial subrange. The inertial dissipation method is used to determine  $\epsilon$  from

$$S = A \frac{18}{55} \epsilon^{2/3} \kappa^{-5/3} \quad (7)$$

where  $S$  is the one-dimensional wave number spectrum of the turbulent velocity,  $\kappa = 2\pi f/V$  is the wave number,  $V$  is the mean current,  $f$  is the frequency, and  $A$  is taken to be 1.5.

[27] Measurements of the turbulent dissipation rate,  $\epsilon$ , were made in the Biosphere 2 ocean according to the model

for the inertial subrange of the kinetic energy spectrum in (7) using both MAVS and the DopBeam. Assuming an extension of Taylor’s hypothesis of frozen turbulence (e.g., steady current) for unsteady advection (e.g., waves) [*Lumley and Terray*, 1983], the measured frequency spectra of vertical velocity were converted to wave number space by  $\kappa = 2\pi f/V$  and  $\epsilon$  is calculated from (7). A safe lower bound of the inertial range is determined according to the criterion  $\kappa z > 5$ . A reasonable upper bound is determined according to the criterion  $\kappa L < 1$ , where  $L$  is the length scale of the sample volume. Before calculating the dissipation rate, the depth-averaged velocity is removed from each bin of the DopBeam to effectively remove the velocity signal due to the waves. In this mode of calculation, the DopBeam gives a profile of dissipation rate up to just beneath the surface while the MAVS gives an estimate of  $\epsilon$  at a fixed depth of 50 cm. The DopBeam can also be used to measure  $\epsilon$  directly from the wave number spectrum in (7) [*Veron and Melville*, 1999] without the need for Taylor’s hypothesis. Comparison of these two distinct estimates in space-time chunks of 20 cm over 10 min show that the difference between the two estimates is within 10% for dissipation rates ranging from  $10^{-6}$  to  $10^{-2}$  W kg<sup>-1</sup>.

[28] The DopBeam also characterized the wavefield that existed during Bio2 RainX III by using the high signal return of the water surface as an estimate of the surface wave elevation. It measured the instantaneous surface elevation to within  $\pm 1.2$  cm at a sample frequency of 20 Hz. Measurements were made continuously whenever the DopBeam was operational. Significant wave height was calculated from the RMS of the surface elevation and the dominant wave frequency was determined as the peak in the power spectra of surface elevation. The high signal return of the water surface was also used to estimate the bulk rain rate for the whole reservoir by taking the increase in distance to the water surface over time. The nominal value throughout all rain events was a significant wave height  $H_s$  of 2.45 cm and a peak frequency  $f_p$  of 0.21 Hz.

## 2.6. Active Controlled Flux Technique

[29] Analogous to gases that move through the surface boundary layer by diffusion, a net heat flux occurs through the aqueous thermal boundary layer (TBL) by molecular conduction at the surface [*Katsaros*, 1980; *Robinson et al.*, 1984]. Because of evaporation, the temperature at the water surface, or skin, is typically less than the bulk temperature immediately below by several tenths of a degree Celsius [*Donlon and Robinson*, 1997; *Schlüssel et al.*, 1990; *Wick et al.*, 1996].

[30] By measuring the fine-scale horizontal structure in skin temperature, passive infrared (IR) imagery is used to explore the impact of turbulence at water surfaces within the TBL. The thickness of the aqueous thermal boundary layer is of  $O(10^{-2} - 10^{-3})$  m [*Hill*, 1972; *McAlister and McLeish*, 1969; *Wu*, 1971]. However, the optical depth of the infrared radiation detected, on average 35  $\mu$ m for the spectral wavelength band of 3–5  $\mu$ m [*Downing and Williams*, 1975; *McAlister and McLeish*, 1970], is much less than the TBL thickness. Therefore, an IR imager is ideally suited to measure the skin temperature and turbulent disruptions of the TBL. Large-scale wave breaking [*Jessup et al.*, 1997], microbreaking [*Zappa et al.*, 2001, 2004], near-surface shear,

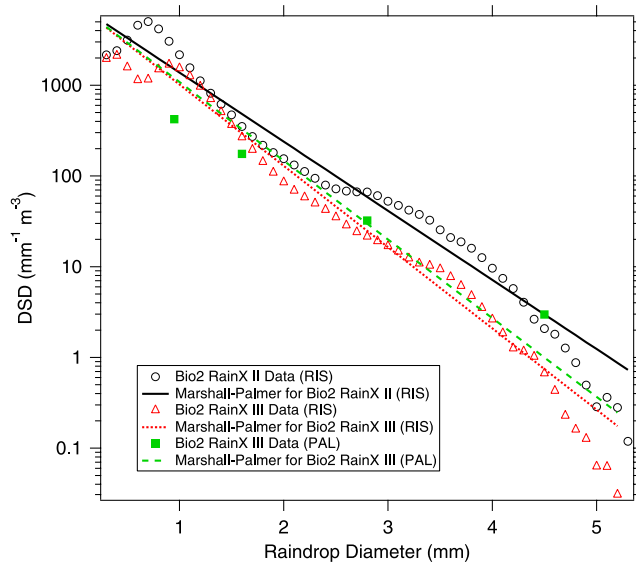


**Figure 2.** Raindrop size distribution (DSD) measured by RIS and PAL during RE4, as well as the Marshall-Palmer DSD. Relative to natural rain, the simulated rain at Biosphere 2 during RainX III tends to be enhanced for small drops (0.75–1.5 mm) and larger drops (3.0–4.0 mm) but deficient for moderate drops (between 1.5 and 3.0 mm) according to the RIS. DSD by RIS from RainX II is also shown for comparison. RainX II DSD shows consistently more drops of every diameter except between 1 and 2 mm where the DSD are roughly the same.

and free-convective patchiness [Zappa *et al.*, 1998] are all turbulent processes that produce signatures of thermal variability quantified by IR imaging techniques. Likewise, turbulence generated by rain impinging on the air-water interface dominates the disruption of the TBL by an enhancement of surface renewal [Craeye and Schlüssel, 1998; Schlüssel *et al.*, 1997]. Thus, IR measurements of the TBL provide the means to remotely examine turbulence interacting with the free surface.

[31] An IR imaging system was used to visualize the turbulence within the TBL generated by the rain and to implement the ACFT. The infrared measurements were made using an Amber model Radiance HS infrared imager (Amber Engineering, Goleta, CA) that responds to radiation in the spectral band of 3–5  $\mu\text{m}$ . It was mounted 9.5 m above the ocean at an incidence angle of roughly  $20^\circ$  to the surface. This configuration resulted in roughly a  $2 \times 2$  m image size with smaller than 1-cm resolution, and the IR imagery was digitized at a frequency of 30 Hz. A nonuniformity correction and a calibration were performed before each run during the experiment using a Santa Barbara Infrared model 2004S blackbody (SBIR, Santa Barbara, California). The noise equivalent temperature difference (or mean resolvable temperature difference) was determined to be  $\pm 0.02^\circ\text{C}$  using the isothermal blackbody calibration target.

[32] The active controlled flux technique (ACFT) relies on heat as a proxy tracer for gas according to unsteady diffusion combined with surface renewal theory to estimate  $k$  [Asher *et al.*, 2004; Atmane *et al.*, 2004; Zappa *et al.*, 2004]. With the ACFT, the water surface is heated with a  $\text{CO}_2$  laser to produce a spot with a measurable temperature difference that can be

tracked within a sequence of infrared images. A Synrad model G48-2-28(W) continuous-wave 25-W  $\text{CO}_2$  laser operating at 10.6  $\mu\text{m}$  was directed at the water surface from above the Biosphere 2 ocean using a series of 5-cm diameter IR mirrors, and was pulsed for 10 ms with a gating frequency of roughly 0.25 Hz. The laser beam generated heated spots on the water surface in the field of view of the infrared imager roughly 7–8 cm in diameter. For the runs used to determine the decay time from the CFT, the infrared imagery was digitized at a frequency of 30 Hz.

[33] The transfer velocity of heat,  $k_H$ , is determined from the surface renewal rate,  $\lambda$ , which is estimated from the thermal decay of the heated spot as predicted from a surface renewal model. The method employed by Haußecker *et al.* [1995] fits the normalized surface temperature,  $T_N$ , of the patches tracked by the ACFT to

$$T_N = \frac{h}{\sqrt{h^2 + 4\alpha t}} e^{-\lambda t} \quad (8)$$

where  $h$  is the penetration depth and  $\alpha$  is the thermal diffusivity of water. The heat transfer velocity is calculated directly from  $\lambda$  using

$$k_H = \sqrt{\alpha \lambda} \quad (9)$$

where the functional form of (9) is specific to a surface renewal model where the probability distribution of the surface element lifetimes is defined by an exponential distribution [Danckwerts, 1951]. Jähne *et al.* [1989] have asserted that the gas transfer velocity,  $k$ , should scale directly to the transfer velocity of heat by

$$k = k_H \left( \frac{Sc}{Pr} \right)^{-n} = k_H (Le)^{-n} \quad (10)$$

where  $Pr$  is the Prandtl number of heat, and  $Le$  is the Lewis number. According to the scaling predicted by (10), previous ACFT laboratory measurements yield values of  $k_H$  that, when scaled to a common value of  $Sc$ , agree with  $k$  measured using conventional gaseous tracers [Haußecker *et al.*, 1995; Jähne *et al.*, 1989]. A limitation of the technique may be that not all eddies that affect the MBL and renew the surface are complete and instantaneous. More recent field and laboratory studies have led to improvements in the technique [Asher *et al.*, 2004; Atmane *et al.*, 2004; Zappa *et al.*, 2003, 2004] and to the suggestion of modeling  $k$  using penetration theory [Harriott, 1962] rather than surface renewal when implementing ACFT. The choice of  $n$  is difficult to determine in natural systems when using this technique. ACFT ideally should be complemented with a tracer technique [Clark *et al.*, 1994], as has been done here, or another suitable method for determining the gas transfer.

### 3. Results

#### 3.1. Rain Rate and Drop Size Distribution

[34] During Bio2 RainX III, RIS, measured DSDs for RE1, RE2, and RE4, respectively. The DSD for RE4 is derived from more than 50,000 drops, and is shown in Figure 2. As commonly observed in natural rain, the DSD reveals that

**Table 1.** Summary of Rain Rate Conditions During Bio2 RainX III<sup>a</sup>

Rain Event	YSI	DopBeam	Buckets	PAL Inversion	PAL Single $f$	RIS
1	39.5	43.0	49.5	30.9	44.4	77.0
2	47.7	60.3	75.0	43.4	52.4	80.1
3	24.3	28.8	35.3	32.9	48.4	N/A
4	30.8	31.9	38.2	33.3	46.9	28.7

<sup>a</sup>All units are in  $\text{mm h}^{-1}$ .

the drop density decreases with increasing drop size. The drop size range measured by the RIS and therefore used to compute rain rates and KEFs was from 0.3 to 5.3 mm diameter. The DSD according to the Marshall-Palmer (M-P) distribution [Marshall and Palmer, 1948] is also shown in Figure 2. This allows for the comparison of the simulated rain to natural conditions. The M-P distribution is given by

$$N(D) = N_0(R) \exp(-\Lambda D) \quad (11)$$

where  $N_0 = 8 \times 10^4 \text{ m}^{-3} \text{ cm}^{-1}$  and  $\Lambda = 42.3 \times R^{-0.214} \text{ cm}^{-1}$  from Olsen *et al.* [1978] are used because  $R$  between model input and output is conserved. The DSD measured during RE4 by RIS shown in Figure 2 closely resembles the M-P DSD. However, some small differences highlight the variability in the simulated DSD. The simulated rain tends to be deficient in drops smaller than 0.75 mm and in the size range of 1.5–3 mm, and tends to be enhanced for drops in the size range of 1–1.5 mm and 3–4 mm. DSD by RIS from RainX II is also shown for comparison. RainX II DSD shows consistently more drops of every diameter except between 1 and 2 mm where the DSD are roughly the same. Analysis of the RIS DSDs indicates that using the M-P DSD instead of measured DSDs would only underestimate the KEF by 4.1%.

[35] The DSD from PAL inversion in Figure 2 is shown to underestimate the RIS DSD for 1.0 mm drops and overestimates the RIS DSD for 4.5 mm drops. The PAL inversion is based on four raindrop categories of special acoustic signatures. These few large bin sizes similarly can lead to deviation from the Marshall-Palmer distribution and the estimated rain rate. Note also that the inversion matrix for PAL was developed empirically according to field data in a freshwater pond in Florida. The study at Biosphere 2 was the first attempt to invert the DSD from laboratory PAL data in a saltwater environment. PAL provides a circular footprint of the surface whose radius is roughly 3 times the depth. For Biosphere 2, PAL was at a depth of 6.5 m and its footprint was  $\sim 20$  m. Also, the geometry of the confined Biosphere 2 ocean can produce resonant sound (increased sound level) which could affect the accuracy of DSD inversion and its relation to the Marshall-Palmer distribution as well as the rain rate.

[36] All the estimated rain rates are summarized in Table 1. Rain rates determined from the YSI pressure probe, the DopBeam, the buckets, the PAL Inversion, the PAL Single  $f$ , and RIS. The YSI and DopBeam estimates of the rain rate are intrinsically a basin-wide mean estimate and on average are within 12% of each other for all experiments. RE1 and RE4 show the closest agreement between the YSI and DopBeam since the duration of these experiments allowed for significant accumulation in the ocean basin. The buckets provide multiple local estimates scattered throughout the

basin while the RIS provide single point measurements of the rain rate. These local estimates are summarized in Table 2 and suggest considerable spatial variability. Additionally, the standard deviation among the buckets for a given rain event ranges from 17.2% to 32.1%. The observed variability in rain rate over the ocean basin is likely due to irregularities in the rain generation system itself as discussed by Ho *et al.* [2004].

[37] Although the bucket, PAL, and RIS data provided estimates of the average rain rates, the considerable spatial variability heterogeneity called for a more consistent method to derive average rain rates. Therefore, the YSI and DopBeam have been used to provide the baseline basin-averaged rain rates. The DSD measured by RIS is assumed to hold over the entire ocean and scaled by the average rain rate, so the spatially averaged global ocean KEFs were  $0.19 \pm 0.02 \text{ J m}^{-2} \text{ s}^{-1}$  and  $0.31 \pm 0.02 \text{ J m}^{-2} \text{ s}^{-1}$  for RE4 and RE1, respectively. Likewise, local rain rates are used to scale these global KEFs to local transfer velocities and dissipation rates later in the Results and Discussion.

### 3.2. Gas Transfer Velocity

[38] The observed  $\text{SF}_6$  concentration in the Biosphere 2 ocean decreases rapidly with the onset of rain. Contrary to Bio2 RainX II [Ho *et al.*, 2004], where part of the effect is due to dilution of  $\text{SF}_6$  tagged ocean water with  $\text{SF}_6$ -free rainwater, during Bio2 RainX III, rainwater actually added  $\text{SF}_6$  to the ocean. The dilution corrected data is shown in Figure 3. With the onset of rain,  $\text{SF}_6$  is quickly lost from the surface layer ( $< 100$  cm) because of enhanced air-sea gas exchange. The combined effect of the wave generator, circulation pumps, and rain caused the  $k(600)$  to be  $34.9 \pm 6.2 \text{ cm h}^{-1}$  for RE4. The  $k(600)$  for no rain conditions in previous experiments at Biosphere2 during RainEx II was  $11.2 \pm 0.3 \text{ cm h}^{-1}$  [Ho *et al.*, 2004].

**Table 2.** Individual Rain Rate Conditions as Measured by the 10-cm Buckets During Bio2 RainX III<sup>a</sup>

Location	RE1	RE2	RE3	RE4
1	60.2	79.2	32.2	19.4
2	59.8	96.8	53.4	36.3
3	38.1	57.2	27.6	28.3
4	51.7	70.4	35.0	36.6
5	48.2	–	29.4	33.3
6	48.2	–	33.1	54.9
7	33.4	30.8	18.4	33.8
8	53.6	–	19.3	20.5
9	52.4	105.6	51.5	59.9
10	54.4	88.0	43.3	44.1
11	35.3	–	35.9	40.5
12	47.0	70.4	38.7	–
13	57.1	90.2	48.8	52.4
14	53.6	61.6	27.6	36.6

<sup>a</sup>All units are in  $\text{mm h}^{-1}$ . For cases when the buckets tipped over during the rain event, no data were recorded. The RIS is nearest to location 5. The DopBeam is nearest to location 11.

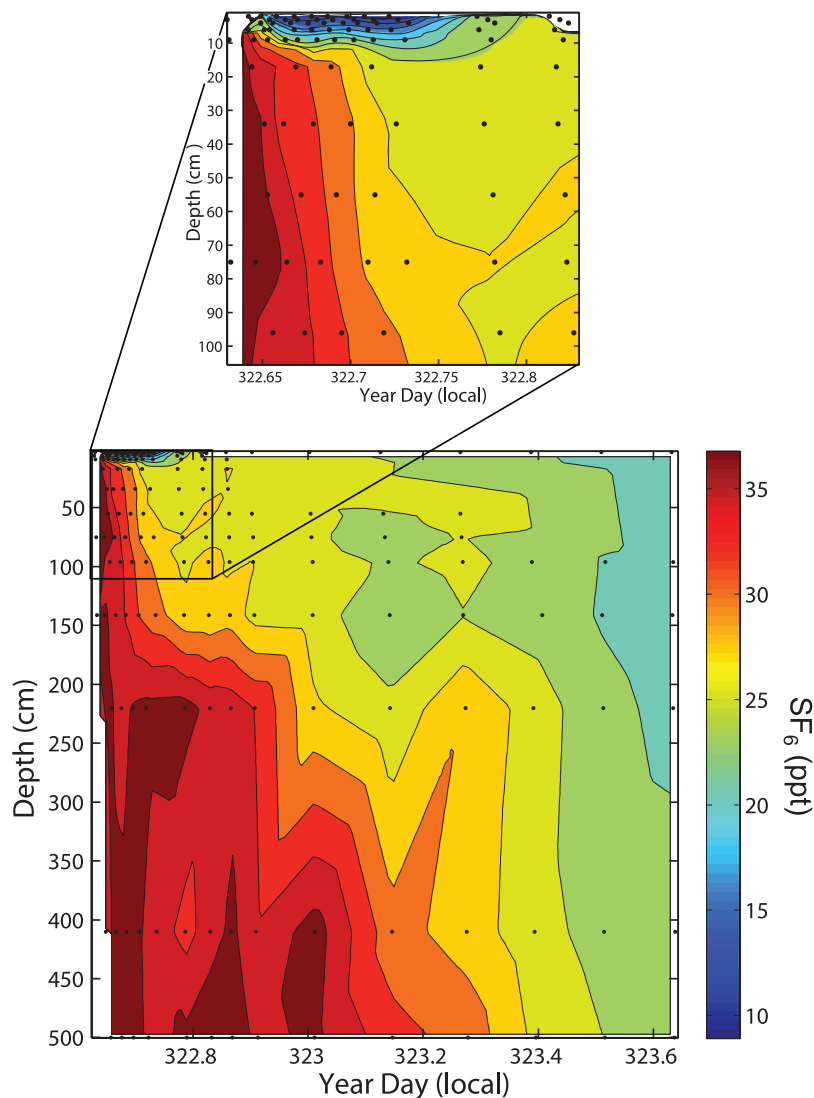


**Figure 3.** Depth measurements of SF<sub>6</sub> concentration as a function of time during RE4. The inset is an enlargement of the top 100 cm of the ocean during the rain event. Each black dot denotes a sample. SF<sub>6</sub> concentration has been corrected for dilution according to equation (2).

### 3.3. High-Resolution Air-Water Transfer Rates and Near-Surface Turbulence

[39] The SF<sub>6</sub> tracer gives a temporally averaged basin-wide gas transfer velocity. Measurements of the transfer velocity by ACFT allow one to examine the temporal behavior of the processes driving the exchange. The magnitude of  $k$  measured by ACFT was comparable for all four rain events during Bio2 RainX III. Figure 4a shows a time series of the transfer velocity,  $k_H(600)$  determined by ACFT referenced to  $Sc = 600$  spanning before, during and following RE1. Both 30 s and 5 min averages for  $k_H(600)$  are given in Figure 4a. Before RE1 begins,  $k_H(600)$  is  $13.5 \text{ cm h}^{-1}$ . As soon as the rain begins,  $k_H(600)$  rises quickly to  $27 \text{ cm h}^{-1}$  and plateaus around  $33\text{--}34 \text{ cm h}^{-1}$ . As the rain continues,  $k_H(600)$  begins to drift down to an equilibrium level around  $30 \text{ cm h}^{-1}$ . At the completion of RE1,  $k_H(600)$  returns to its pre-RE1 level of  $12 \text{ cm h}^{-1}$ .

[40] Measurements of  $k_H(600)$  for RE4 are shown in Figure 5a and exhibit similar characteristics to RE1.  $k_H(600)$

abruptly increases at the onset of the rain event from the non-rain value of  $12.7 \text{ cm h}^{-1}$ . In the early stages of RE4,  $k_H(600)$  varies between 24 and  $26 \text{ cm h}^{-1}$ , and as the rain continues  $k_H(600)$  increases slightly and stabilizes at  $27 \text{ cm h}^{-1}$ . At the end of RE4,  $k_H(600)$  returns to its pre-RE4 level.

[41] Near-surface turbulence is thought to be responsible for air-sea gas transfer, and  $k$  has been modeled and shown to scale with  $\varepsilon^{1/4}$  [Lamont and Scott, 1970]. Figure 4b shows the temporal evolution in turbulence dissipation rate as a function of depth at the beginning, during, and end of RE1 in the Biosphere 2 ocean. The calculation of  $\varepsilon$  is described above. Prior to the beginning of RE1, background  $\varepsilon$  levels measured at roughly 50 cm depth with the MAVS were  $5 \times 10^{-6}$  to  $1 \times 10^{-5} \text{ W kg}^{-1}$ . As the rain begins, the surface value of  $\varepsilon$  increases abruptly by several orders of magnitude to  $1.0 \times 10^{-2} \text{ W kg}^{-1}$ . The turbulent dissipation rate decays significantly with depth to levels of  $3.0 \times 10^{-5} \text{ W kg}^{-1}$  at a depth of 25 cm. Surface values of  $\varepsilon$  remain above  $1.0 \times 10^{-3} \text{ W kg}^{-1}$  for nearly an hour. Following the peak plateau,  $\varepsilon$  decreases to

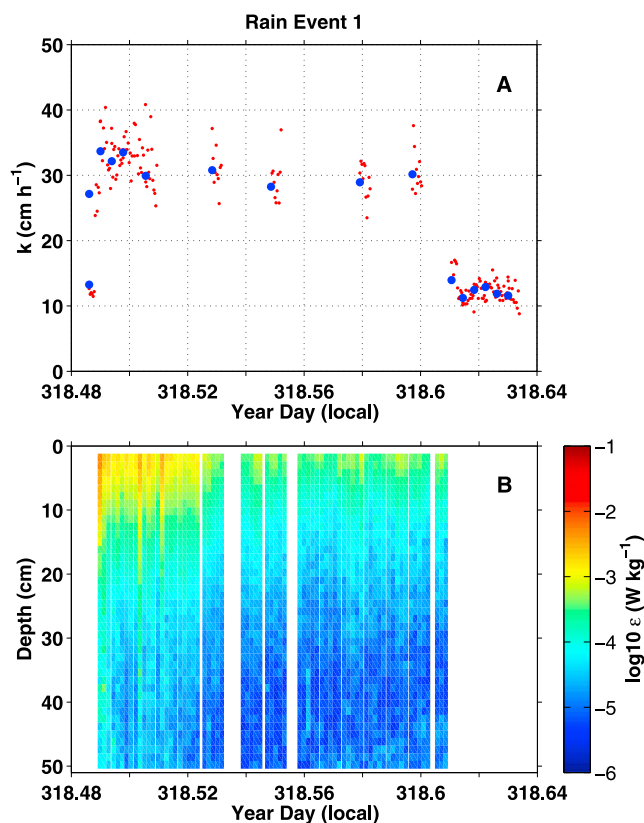


**Figure 4.** (a) Time series of the transfer velocity  $k_H(600)$  determined by ACFT referenced to a Schmidt number of 600 spanning before, during, and following RE1. The red dots are 30-s averages, and the large blue dots are 5-min averages. (b) Temporal evolution of turbulence dissipation rate  $\varepsilon$  as a function of depth at the beginning, during, and end of RE1 in the Biosphere 2 ocean.

an equilibrium level of  $3 \times 10^{-4} \text{ W kg}^{-1}$  until the rain terminates. The variability of  $\varepsilon$  at this single location is significant.

[42] Measurements of  $\varepsilon$  during RE4 are shown in Figure 5b. Note that the circulation pumps are running during RE4 that adds to the background turbulence. As a result, the turbulent dissipation rate throughout the bulk fluid stays nearly constant at  $3.0 \times 10^{-5} \text{ W kg}^{-1}$ . As the rain begins, the turbulence at the surface increases above background levels to roughly  $3.0 \times 10^{-4} \text{ W kg}^{-1}$ . Surface values of  $\varepsilon$  increase to an equilibrium level of  $2 \times 10^{-3} \text{ W kg}^{-1}$  until the rain terminates. Both  $k_H(600)$  and  $\varepsilon$  track each other very well and suggests a causal relationship between the turbulence generated by rain impinging at an air-water interface and the air-water gas exchange rate.

### 3.4. High-Resolution Temperature and Salinity Profiles

[43] Figure 6 shows the temporal evolution in ocean temperature, salinity, density and the Brunt-Väisälä frequency squared,  $N^2$ , as a function of depth at the beginning, during and end of RE1 in the Biosphere 2 ocean. The calculation of  $N^2$  is determined from  $(g/\rho_o)(d\rho/dz)$  where  $g$  is the acceleration due to gravity,  $\rho_o$  is the reference density, and  $d\rho/dz$  is the density gradient.

[44] Before the start of RE1, the density was homogeneous throughout the water column on the basis of previous observations (not shown) [see *Ho et al.*, 2004]. The presence of the rain had a delayed effect on the surface layer, where a fresh, warm lens developed after just under an hour into the rain event. Localized, instantaneous stratification is likely to have been present early during RE1, but it was not measurable. During RE1, the salinity dropped from an initial value of 35.7 to a minimum of 32.5; the initial temperature was  $25.6^\circ\text{C}$ , and reached a maximum of  $25.78^\circ\text{C}$  at the surface. The density is clearly driven by the salinity and drops from an initial value of  $1023.7 \text{ kg m}^{-3}$  to a minimum surface value of  $1021.1 \text{ kg m}^{-3}$ . Most noticeable is the stratification as measured by  $N^2$  showed a distinct gradual deepening roughly an hour into the rain event to a depth of 20 cm. This stratified layer with  $N^2$  values greater than  $0.03 \text{ rad}^2 \text{ s}^{-2}$  lasted for the duration of the rain event. At the completion of the rain event, this stratification level disintegrates while a layer at 1.5 m depth that had developed previous to the end of the rain event strengthens. After the rain ceased, the fresher surface layer continued to mix down into the ocean interior to an asymptotic depth of 3.5 m. Even after 2 full days, the ocean had not re-established its pre-rain state because the pumps had been turned off during this rain event.

[45] Subsequently, RE4 (Figure 7) showed similar behavior to that during the RE1. Here, a fresh, cold lens developed during the rain event. During RE4, the salinity dropped from an initial value of 34.7 to a minimum of 32.8; the initial temperature was  $25.37^\circ\text{C}$ , and reached a minimum of  $25.26^\circ\text{C}$  at the surface. The density again is clearly driven by the salinity and drops from an initial value of

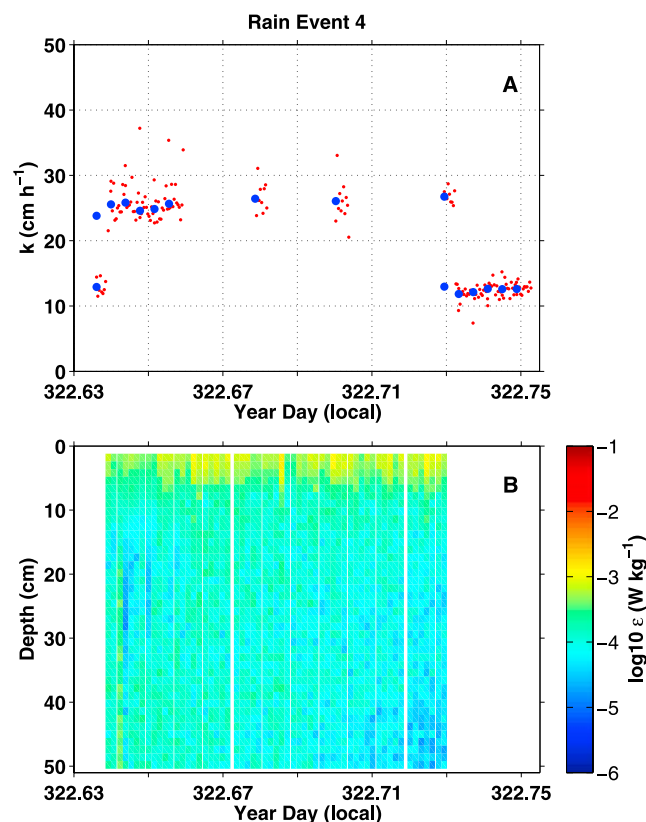


**Figure 5.** Same as Figure 4 for RE4.

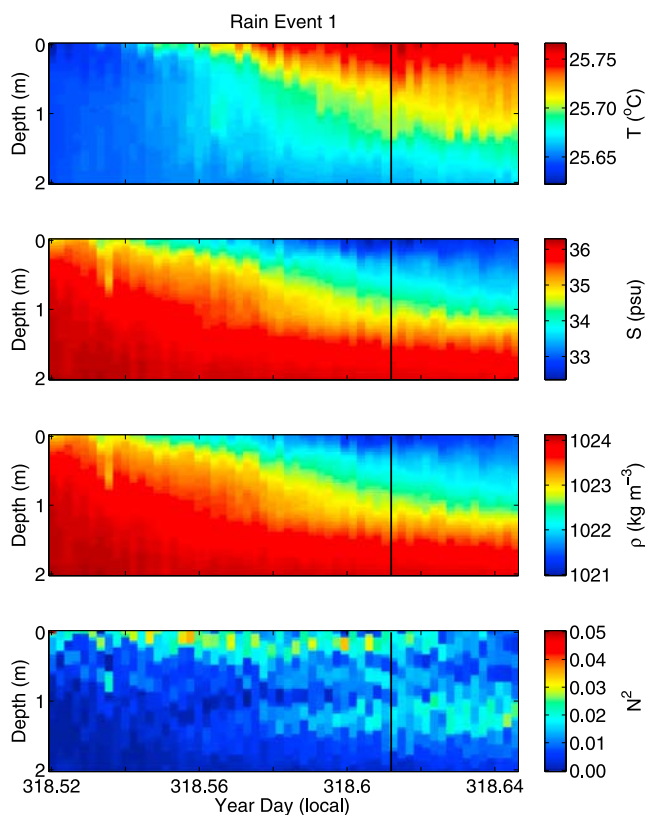


**Figure 6.** Time series plot of the temperature  $T$ , salinity  $S$ , density  $\rho$ , and the Brunt-Väisälä frequency squared,  $N^2$ , from the autonomous profiling MicroCat for RE1 over the upper 2 m of the Biosphere 2 ocean. The calculation of  $N^2$  is determined from  $(g/\rho_o)(d\rho/dz)$ , where  $g$  is the acceleration due to gravity,  $\rho_o$  is the reference density, and  $d\rho/dz$  is the density gradient.

1023.2  $\text{kg m}^{-3}$  to a minimum surface value of 1021.6  $\text{kg m}^{-3}$ . Most noticeable is that the stratification is significantly less than observed during RE1. The stratified layer with  $N^2$  values between 0.02 and 0.03  $\text{rad}^2 \text{s}^{-2}$  becomes evident more than halfway through the rain event and no secondary deeper layer is apparent. This is likely due to the enhanced mixing caused by the circulation pumps. After the rain ceased, the fresher surface layer continued to mix down into the ocean interior to an asymptotic depth of 2.0 m. and the ocean became well-mixed within a day.

## 4. Discussion

### 4.1. Comparison of RainX Gas Transfer Velocities to KEF Relationship

[46] The bulk tracer results presented here confirm the previous finding by *Ho et al.* [2004] that rainfall on the ocean enhances the air-sea gas exchange rate.  $k(600)$  was  $34.9 \pm 6.2 \text{ cm h}^{-1}$  during RE4 with energy input from the wave generator, the circulation pumps, and from rain. The  $k(600)$  for no rain conditions in previous experiments at Biosphere 2 during RainX II was  $11.2 \pm 0.3 \text{ cm h}^{-1}$  [*Ho et al.*, 2004], so the difference in  $k(600)$  between the rain and no rain conditions is  $23.7 \text{ cm h}^{-1}$  at a KEF of  $0.19 \text{ J m}^{-2} \text{ s}^{-1}$ . Note that  $k(600)$  for the RE2 during RainX II was reported incorrectly by *Ho et al.* [2004] and is in fact  $44.6 \pm 5.4 \text{ cm h}^{-1}$ , so the

difference in  $k(600)$  between rain and no rain conditions during RainX II was  $33.4 \text{ cm h}^{-1}$  at a KEF of  $0.37 \text{ J m}^{-2} \text{ s}^{-1}$ . Both the value reported here from RainX III and the updated value from RainX II fall within the bulk relationship shown in Figure 8 between  $k(600)$  and KEF established by *Ho et al.* [2000].

[47] It is likely that bubble-mediated exchange plays a role in the Biosphere 2 saltwater ocean as it did in the freshwater measurements by *Ho et al.* [2000] and will be discussed later. Mean transfer rates from the ACFT for all rain events and one non-rain event are shown in Figure 9a and range between 12.9 and 31.7  $\text{cm h}^{-1}$ . We note a reasonable correlation of  $k_H(600)$  with increasing rain rate (coefficient of determination of 0.987) for the range of values investigated. The  $\text{SF}_6$  evasion and ACFT results showing an increase in transfer velocity due to rain is consistent with the physical measurements of turbulence and stratification made during RE1 and is described in detail in the following section.

### 4.2. Relationship Between High-Resolution Turbulence, Stratification, and Transfer Velocity

[48] The high-resolution transfer rate and turbulence results presented here clearly show the causal relationship between rainfall and air-sea gas exchange. Rainfall impinging on the ocean surface enhances the turbulent dissipation rate, which in turn controls the rate of air-sea gas transfer. Turbulent kinetic energy is generated during the rain events with the impact of each raindrop on the water surface and is

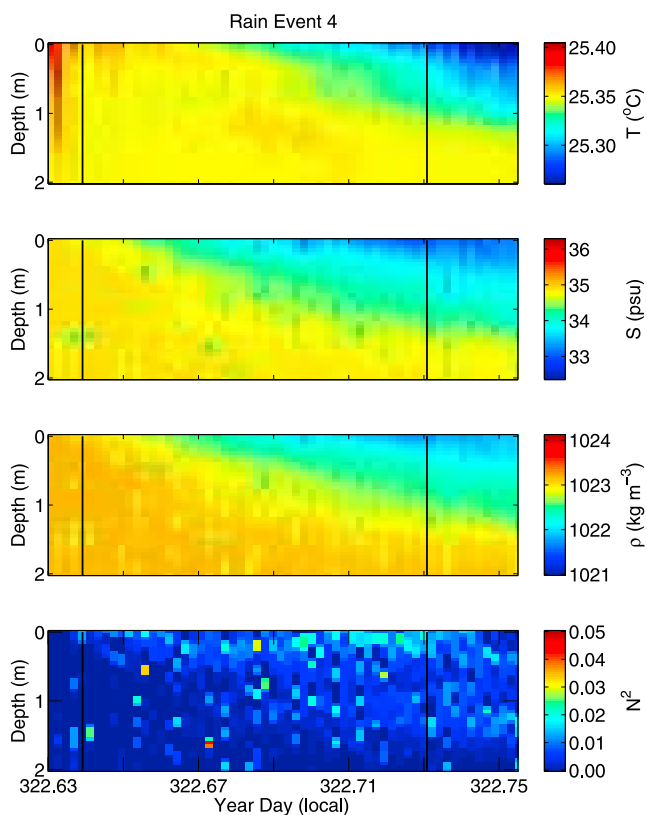


**Figure 7.** Same as Figure 6 for RE4. Note that the color scale for temperature has a range of  $0.15^\circ\text{C}$  as in Figure 6 and that the scales for salinity, density, and  $N^2$  are identical as those presented in Figure 6.

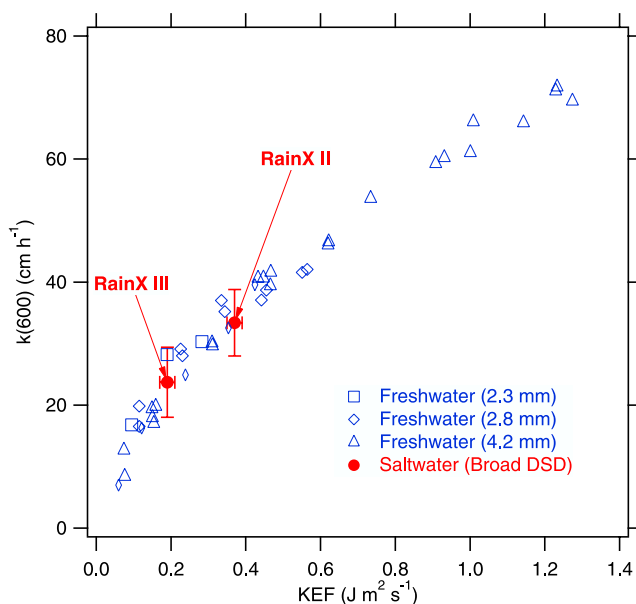


**Figure 8.** Gas transfer velocity versus kinetic energy flux KEF. Freshwater data represent distinct raindrop sizes with diameters of 2.3 mm, 2.8 mm, and 4.2 mm from experiments at the Wallops rain facility and are summarized by *Ho et al.* [2000]. Saltwater data represent broad raindrop size distributions and are from RainX II [see *Ho et al.*, 2004] and this study of RainX III at Biosphere 2.

delivered to the surface layer of the ocean. The cumulative result caused an increase in  $\varepsilon$  (Figures 4b and 5b) and  $k_H(600)$  (Figures 4a and 5a). IR imagery shows that raindrops impacting the water surface generate disturbances of the surface aqueous boundary layer with the horizontal scales of energetic mixing at the surface of  $O(10\text{ cm})$  that are comparable to the vertical scales of mixing during the rain events and observed in previous laboratory studies [*Green and Houk*, 1979; *Lange et al.*, 2000]. Following this increase in  $\varepsilon$  and enhanced transfer rate, stable stratification developed (Figures 6 and 7; increase in  $N^2$ ) because of the addition of freshwater by rain and suppresses turbulent mixing near the surface, causing  $\varepsilon$  to decrease slightly. This stratified interface deepens to roughly 20 cm and effectively traps the enhanced turbulence in the near-surface layer. This forces  $\varepsilon$  and  $k_H(600)$  to remain constant, yet significantly enhanced, for the duration of the rain event. At the conclusion of the rain event, the stratified interface at 20-cm depth disintegrates rapidly,  $\varepsilon$  diminishes to pre-rain event levels, and the transfer rate plummets to the no-rain condition. This stratification that leads to the trapping of  $\varepsilon$  near the surface will not only have a profound effect on the enhanced  $k_H(600)$ , but also will play a role in diminishing the vertical mixing of mass transported to the air-water interface that is important as the driving potential in the flux of gas.

[49] The secondary stratified interface that develops at a depth of 1.25 m during RE1 as observed in Figure 6 suggests that the erosion of the stratified layer has begun even while the near-surface stratified interface at 20-cm depth persists until the rain event has concluded because of the constant supply of freshwater to the layer. This suggests a balance of the KEF input with dissipation in the near-surface layer above

the stratified layer, damping of turbulence by the stratification, and diffusion of turbulent energy via entrainment deepening of the stratified layers. The balance assumes a minimal horizontal advection of energy. The turbulence due to the raindrops significantly enhances mixing. These observations are an interesting first glimpse of an overlapping transition from the rain-driven quasi steady state stratified layer to deepening of this layer by entrainment that initiates at a significantly deeper layer.

[50] During RE4, the circulation pumps were operating and caused significant background turbulence as evidenced by comparison of Figures 4b and 5b. In addition, the warm fresh lens of RE1 produces a statically stable system, while the cold fresh lens of RE4 generates a diffusively unstable system. The diffusively unstable system resulted in slightly

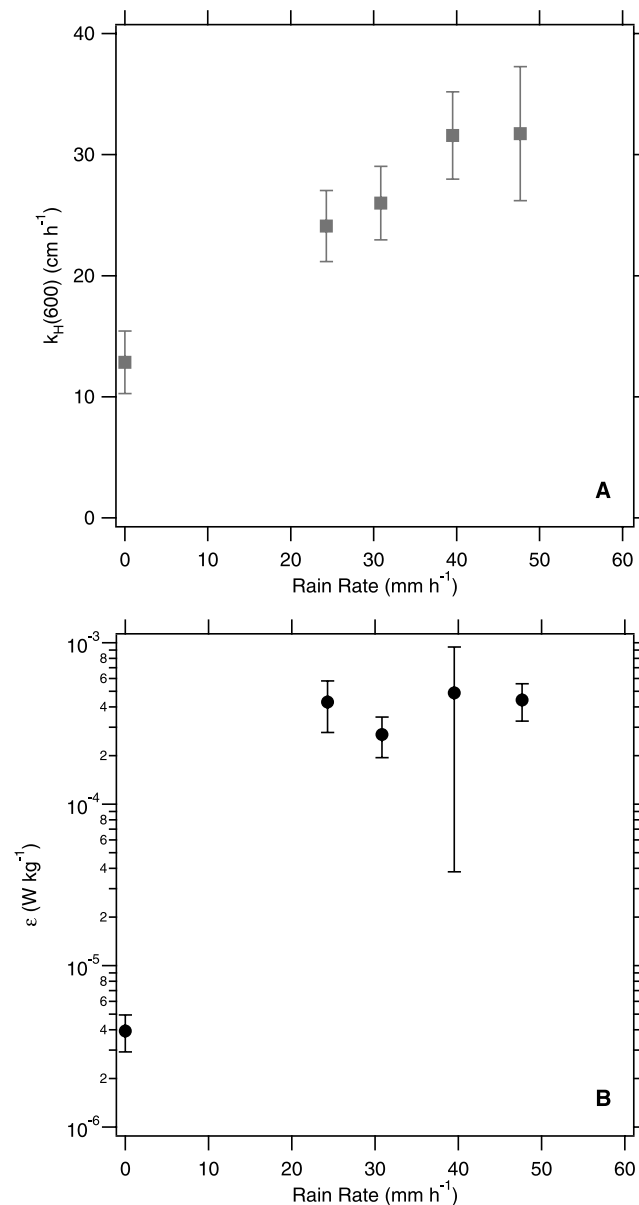


**Figure 9.** (a) The transfer velocity  $k_H(600)$  determined by ACFT referenced to a Schmidt number of 600 and (b) turbulent dissipation rate  $\varepsilon$  both as a function of rain rate.

enhanced surface turbulence over the statically stable system as evidenced by the higher surface values of  $\varepsilon$  and the weaker stratification via  $N^2$ . The higher bulk levels of  $\varepsilon$  and weaker stratification result in a speeding up of the entrainment processes described above that potentially hinder the development of the secondary stratified layer.

#### 4.3. Comparison of Dissipation Rates During RainX Experiments to Breaking Wave Measurements

[51] During Bio2 RainX III, near-surface  $\varepsilon$  ranged from  $10^{-6}$   $\text{W kg}^{-1}$  in the absence of rain to instantaneous levels of  $10^{-2}$   $\text{W kg}^{-1}$  during RE1 as shown in Figures 4b and 5b, and observed for the other rain events. These levels during rain events are  $O(100)$   $\text{W kg}^{-1}$  greater than observed during RainX II because the measurements during RainX III were made at the surface compared to the bulk measurements of RainX II. Sustained mean dissipation rates for all rain events are shown in Figure 9b and range between  $2.7 \times 10^{-4}$  and  $4.9 \times 10^{-4}$   $\text{W kg}^{-1}$ . The mean dissipation rates in Figure 9b were calculated as the average of the top 2 bins during an individual rain experiment. No distinct relationship was found for dissipation rate as a function of rain rate for the narrow band of values investigated. For comparison, estimates of  $\varepsilon$  beneath breaking waves ranged from  $10^{-5}$  to  $10^{-2}$   $\text{W kg}^{-1}$  on the open ocean [Gemmrich and Farmer, 2004] and on lakes [Agrawal et al., 1992; Terray et al., 1996]. The results demonstrate that rain forcing significantly enhances turbulence under no wind conditions in the Biosphere 2 ocean and that near-surface  $\varepsilon$  is comparable to moderate wave breaking. Instantaneous dissipation rates during strong rain events were found to be similar to those found beneath strong breaking waves. Raindrops are ubiquitous, and the uniform surface mixing and subsequent air-water gas exchange are comparable to other dominant processes such as wave breaking.

#### 4.4. Effects of Bubble-Mediated Exchange on RainX Results

[52] Bubble-mediated exchange is an important conduit for air-sea gas transfer [Asher et al., 1996; Keeling, 1993; Woolf and Thorpe, 1991; Woolf, 1993] and is intrinsic to the comparisons between measurements from RainX experiments in the Biosphere 2 saltwater ocean and the experiments performed in freshwater at the Rain-Sea Interaction Facility (RSIF) shown in Figure 8. The bulk KEF relationship of Ho et al. [1997] was developed using the freshwater measurements that included the presence of bubbles at RSIF. The bubble generation characteristics are different in salt water and freshwater systems. Bubble-mediated gas transfer is influenced by the size of the bubbles, the penetration depths of the bubbles, the rise velocity of bubbles, the solubility of the gas, the diffusivity of the gas, and the presence of surfactants. Raindrops generate large bubbles at the surface that remain near the surface without penetrating to deeper than  $O(10)$  cm [Ho et al., 2000]. Each bubble of a particular diameter has an equilibrium depth at which its rise to the surface corresponds to the time it takes for a specific gas to equilibrate completely with the bubble volume and therefore maximize its bubble-mediated gas transfer. Therefore, many small bubbles have an equivalent impact on the transfer velocity as does a significantly fewer number of large

bubbles. Typically, rain on freshwater shows bubble size distributions with many large bubbles but fewer total bubbles, as observed in the data of Ho et al. [2000], since bubbles are more likely to coalesce in freshwater but less so in saltwater [Asher et al., 1997; Scott, 1975]. (Note that large bubbles generated during rain events may not be in close enough proximity to coalesce.) Therefore, it is important to note the difference between the rain data from the freshwater at RSIF and the saltwater ocean in Biosphere 2.

[53] The raindrops in RSIF were distinct sizes of 2.3, 2.8, and 4.2 mm while the raindrops produced in the RainX II and RainX III had broad distributions as shown in Figure 2. Here, there were significantly more smaller drops because of the broad DSD as opposed to the discrete raindrops of 2.3, 2.8, and 4.2 mm by Ho et al. [2000]. The total number of raindrops calculated in each experiment shows that during RainX II and III there were at least 20 times as many raindrops relative to the RSIF experiments at the same KEF. Furthermore, the RSIF data show that for a given rain rate there are significantly more bubbles generated by the 2.8-mm drops than the 4.2-mm ones because the total number of bubbles generated is correlated with the total number of raindrops hitting the water surface. Assuming this linear relationship between the number of raindrops and the number of bubbles, the rain data from the two RainX experiments in Biosphere 2 would be expected to give a higher gas transfer rate compared to the RSIF data because of enhanced bubble-mediated exchange strictly by the difference in DSD. In Figure 8, however, the Biosphere 2 measurements fall within the bands of the RSIF results. An expected increased bubble-mediated component in Biosphere 2 is compensated by a decreased contribution by turbulence because the turbulence is shown in Figures 4 and 5 to diminish during the course of the experiment because of the density stratification and other modifications and transformations to the KEF input that are not present in the RSIF study. Therefore, it is likely that bubble-mediated exchange plays an enhanced role in the Biosphere 2 saltwater ocean compared to the freshwater measurements reported by Ho et al. [2000].

#### 4.5. Scaling of Gas Transfer to Dissipation Rate for RainX Results

[54] Synthesizing all of these individual rain experiments indicates that dissipation rate controls gas exchange for a rain-forced system as hypothesized. According to (1),  $k$  should scale with  $\varepsilon^{1/4}$ . Figure 10 shows  $k(600)$  measured using both ACFT and  $\text{SF}_6$  tracer release for a variety of different rain rates that include both the RainX II [see Ho et al., 2004] and RainX III [see Zappa et al., 2007] data in Biosphere 2 (rain; no wind) to be proportional to the model expressed in (1) with  $n = 1/2$ . Note that in order to compare ACFT and  $\text{SF}_6$  directly in Figure 10, the  $\text{SF}_6$  tracer release has been adjusted to turbulence-only transfer by removing the bubble-mediated exchange ( $\sim 20\%$ ) according to the estimates provided by Ho et al. [2000] and the discussion above regarding the differences in stratification and drop size distribution between Biosphere 2 and RSIF. The results here clearly show that gas transfer scales with  $\varepsilon^{1/4}$  for this system that is dominated by rain and includes effects of waves and artificial background turbulence (i.e., circulation pumps). The constant of proportionality associated with (1) and used

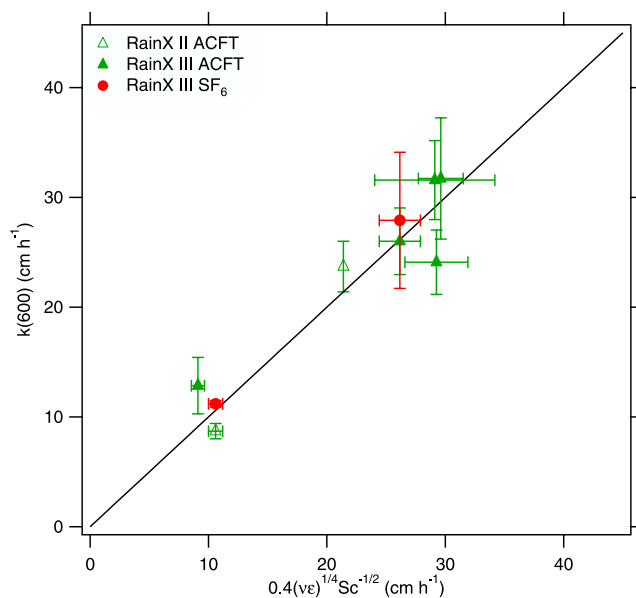


**Figure 10.** Gas transfer velocity from ACFT versus modeled  $k$  as determined from (1) for all rain rates during both RainX II [see *Ho et al.*, 2004] and RainX III at Biosphere 2. The gas transfer measurement using the SF<sub>6</sub> tracer release during RainX III is also shown for comparison.

in Figure 10 was determined by *Zappa et al.* [2007] to be 0.42 for a wide range of measurements that included wind, wave, and tidal forcing. The  $\varepsilon^{1/4}$  scaling shows a higher correlation (coefficient of determination of 0.94) than would be expected from the *Wanninkhof* [1992] quadratic wind speed parameterization, since the process of rain and not wind is driving the near surface turbulence that dominates the transfer. Furthermore,  $\varepsilon$  may prove to be more relevant than KEF in terms of parameterizing gas transfer. The effects of stratification have been shown here to have a dynamic control on the near surface turbulence and  $k(600)$  is correlated strongly with  $\varepsilon^{1/4}$ . While KEF may be relevant to measure the turbulent input to the system during rain events,  $\varepsilon$  at the surface is the most relevant response to all the modifications and transformations to the turbulent state that occur.

#### 4.6. Effectiveness of ACFT in Non-Wind-Forced Conditions

[55] The direct comparison of  $k(600)$  for ACFT to SF<sub>6</sub> tracer release in Figure 10 shows that the gas transfer velocity determined from the ACFT and the SF<sub>6</sub> tracer release are within measurement error. Similar results were found for the comparison between  $k(600)$  determined from ACFT and atmospheric CO<sub>2</sub> profiles in the Parker River Estuary [*Zappa et al.*, 2003] where bed-driven turbulence dominated the gas transfer instead of the wind. Both the Biosphere 2 and Parker River results provide evidence for the usefulness of ACFT under conditions that are not those found during strongly forced wind-driven laboratory [*Atmane et al.*, 2004] and field [*Asher et al.*, 2004] experiments. This discrepancy suggests that there is a distinct difference between the transfer forced by wind and that forced by bed-generated or rain-induced turbulence, i.e., sheared versus zero-mean sheared environments.

#### 4.7. Importance of Surface Dissipation Rates in Air-Sea Gas Transfer

[56] An underlying assumption in (1) is that  $\varepsilon$  is measured directly at the water surface. Since the profile of turbulence near the air-water interface may be complicated by the interplay between rain, wind, waves, current shear and other processes (namely stratification), measurements at depth will not be representative of  $\varepsilon$  at the surface because the profile changes nonlinearly with environmental forcing. The uppermost dissipation measurements during the rain experiments at Biosphere 2 were made within a few centimeters of the surface using the DopBeam. Figures 4 and 5 demonstrate that the surface turbulence is crucial to gas transfer since  $k_H(600)$  tracks  $\varepsilon$  (at  $z = 2.5$  cm) regardless of the variability in turbulent dissipation rate that occurs in the bulk fluid. The comparison of measured and modeled  $k$  using (1) for the Biosphere 2 data show little variability in Figure 10 and even less variability when compared to previous results [*Zappa et al.*, 2007] across a variety of systems (i.e., estuaries, rivers, and coastal ocean) and environmental forcings (i.e., wind, wave, and tides). This small variability in Figure 10, even in the presence of significant salinity stratification developed from freshwater rain on the saltwater ocean, strengthens the case for an  $\varepsilon^{1/4}$  scaling. Nonetheless, some of the scatter in Figure 10 may be due to the significant spatial variability in the rain distribution in these studies.

[57] The DopBeam data shown in Figure 11 gives a profile of dissipation rate near the air-water interface averaged over the beginning 10 min of RE1 from Figure 4b. This profile is representative of all profiles that show an  $e^{-z}$  dependence, where  $z$  is depth positive downward. This dependence is analogous to that suggested by *Anis and Moum* [1995] that high levels of turbulent kinetic energy at the surface, in this case generated directly by rain, are transported downward away from the surface by the motion of waves in the model ocean. Measurements of dissipation rate just below the surface are more than an order of magnitude higher than those a few tens of centimeters below. Magnitudes of bulk  $\varepsilon$  at Biosphere 2 have remained roughly constant during RainX II and III. The measurement of  $\varepsilon$  at 25-cm depth from the DopBeam is nearly identical to that found using a single point acoustic Doppler velocimeter (ADV) sampling at 25-cm depth in the same model ocean under similar conditions [*Ho et al.*, 2004].

#### 4.8. Modeling the Near-Surface Dissipation Rate Profile During Rainfall

[58] Given the importance of using the dissipation rate at the surface for modeling gas transfer and the nonlinear near-surface profile of turbulence observed beneath rainfall that routinely decays by more than an order of magnitude over 50 cm, modeling of this  $\varepsilon$  profile will have an important impact on future climate studies that involve rain-induced gas exchange. The primary effect of rain falling on an open body of water is to impose a distributed turbulent kinetic energy flux at the surface. The subsurface turbulence generated by the impacting droplets then diffuses downward, creating a turbulent kinetic energy (TKE) dissipation rate profile with depth. For modeling purposes, it is assumed that any vertical circulation induced in the water column is negligible, as is borne out by observations.

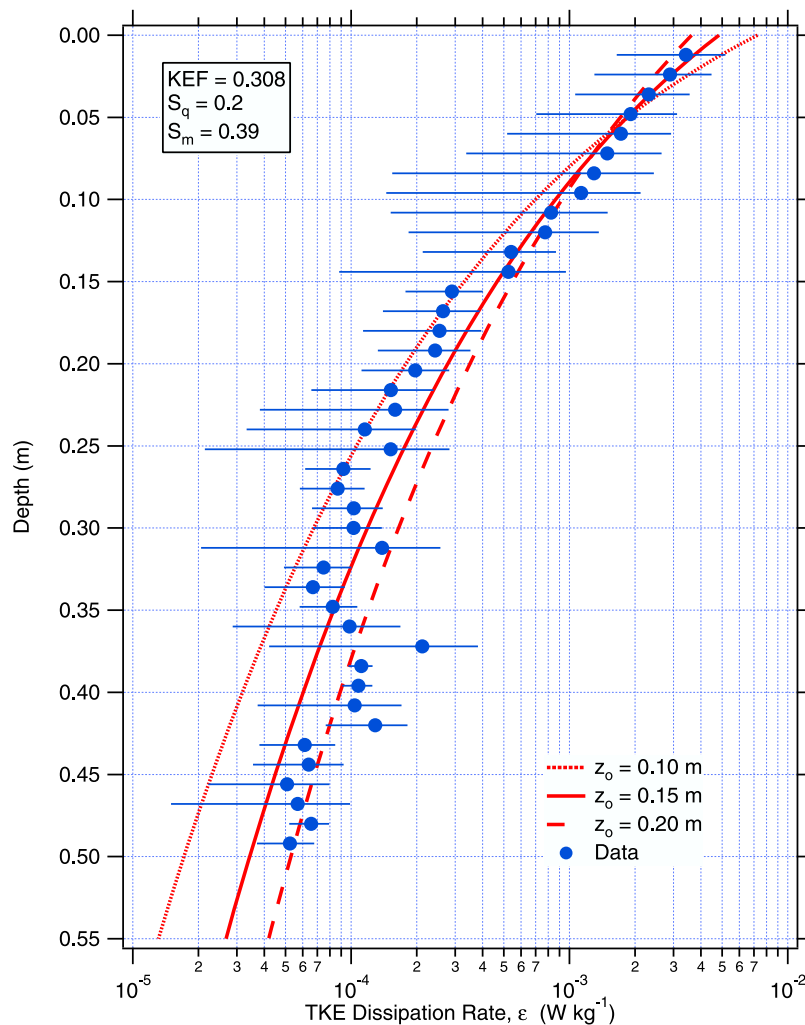


**Figure 11.** Depth profile of dissipation rate for RE1 determined using the DopBeam directed vertically at the surface of the model ocean in the Biosphere2 Center. The data have been averaged for roughly the first 11 min in Figure 4b, and the bars denote the variability during the averaging time. The bulk rain rates are tabulated in Table 1. Because of spatial variability in the rain rate from experiment to experiment, the local dissipation rates may vary significantly. The red traces show the profile results from the Craig-Banner model using the measured KEF and assuming the standard Mellor-Yamada coefficients for  $z_o$  values of 0.15 m, 0.20 m, and 0.25 m for RE1.

[59] A straightforward extension of the model of *Craig and Banner* [1994] is used here for the first time to model the influence of rainfall on the near-surface TKE budget. This model was originally introduced to explore the influence of breaking wave turbulence on upper ocean currents. The Craig-Banner (CB) model assumes a flat sea surface, and horizontal momentum equations that use an eddy viscosity determined by a Mellor-Yamada 2 1/2 turbulence scheme [Mellor and Yamada, 1982]. Here, the eddy viscosity is proportional to the mixing length and the turbulent kinetic energy, and is determined by a turbulent kinetic energy equation representing a balance between parameterized versions of diffusion, dissipation and shear generation of turbulence. At the sea surface, we impose a surface turbulent kinetic energy input rate associated with the incident rain.

[60] In the present application, the input water-side friction velocity was set to a negligibly small level ( $10^{-5}$  m/s), and

the surface TKE flux, now independent of the friction velocity, is prescribed by the measured value. The energy and momentum diffusion coefficients  $S_q$  and  $S_m$  were set to the standard Mellor-Yamada values of  $S_q = 0.20$  and  $S_m = 0.39$ , and the sensitivity of the results to these choices was checked. The water-side roughness length  $z_o$  was varied over the range from 0.10 to 0.20 m, consistent with the observed turbulence penetration depth in the initial 10 min rainfall period before stratification effects came into play. The model depth was set to 200 m to simulate deep-water conditions.

[61] For the given input TKE flux ( $\text{KEF} = 0.308 \text{ J m}^{-2} \text{ s}^{-1}$  for RE1; a small fraction is potentially lost because of the formation of the bubble cavity and is assumed to be gained back from the turbulent wake of the bubble during the buoyant rise to the surface (F. Veron, personal communication, 2008)) and roughness length, the TKE dissipation rate profile with depth was calculated and compared with the

measured initial profile. The CB model results are shown in Figure 11 with the measurements of  $\varepsilon$ . Figure 11 shows that the standard Mellor-Yamada coefficients for the imposed choice of  $z_o = 0.15$  m provides a close agreement of the CB model results to the observations of  $\varepsilon$  over most of the uppermost 0.5 m of the water column. The sensitivity of the results to different choices of  $z_o$  (0.10 and 0.20 m) is indicated. Least squares regression between the CB model results and the measurements of turbulent dissipation rate gives a slope of 1.01 for  $z_o = 0.15$  m as opposed to 1.21 and 0.85 for  $z_o = 0.10$  m and 0.20 m, respectively. Furthermore, the root-mean square (RMS) difference between the CB model results and the measurements of  $\varepsilon$  was  $9.9 \times 10^{-5} \text{ W kg}^{-1}$  for  $z_o = 0.15$  m as compared to  $3.0 \times 10^{-4} \text{ W kg}^{-1}$  and  $1.5 \times 10^{-4} \text{ W kg}^{-1}$  for  $z_o = 0.10$  m and 0.20 m, respectively. Both the least squares regression and the RMS difference support a  $z_o = 0.15$  m for this data set. The sensitivity of the model to varying  $S_q$  and  $S_m$  was also explored. Reducing  $S_q$  by half required increasing  $z_o$  to 0.2 m for the closest fit. Likewise, doubling  $S_q$  required decreasing  $z_o$  to 0.1 m. Similar variations in  $S_m$  had minimal effect, as expected in this quasi-static flow.

[62] *Gemmrich and Farmer* [1999] estimate  $z_o$  from profiles of temperature fluctuations beneath breaking waves. They used a Prandtl-type mixing model to find a linear increase in eddy sizes with distance from the interface, resulting in a  $z_o$  of 0.2 m. Effectively, this  $z_o$  describes the region near the surface that is well mixed and is similar to the near-surface layer in the Biosphere 2 ocean. They also observed that bubbles generated by breaking waves produced a layer that penetrated down to 20 cm during these same measurements of  $z_o$ . Similarly, rain provides an input to the near surface ocean comparable to breaking waves and the choice of  $z_o$  used in the Craig-Banner model is consistent with *Gemmrich and Farmer* [1999] and with the observations of the depth of stratification.

[63] Thus, the exploratory efforts to use the Craig-Banner model to infer the dissipation rate profile are very encouraging. This approach has the capability to account for the observed dissipation rate profile once the KEF and  $z_o$  are specified. Prescribing the rainfall KEF alone is insufficient to predict the resulting turbulent dissipation rate near the surface. The sensitivity of the model estimates was assessed for a range of plausible estimates of  $z_o$  using standard  $S_q$  and  $S_m$  settings. It was found that the surface dissipation values were not very sensitive to the choice of  $z_o$ , varying by less than a factor of 2 for a factor of 2 change in  $z_o$ . Given the  $\varepsilon^{1/4}$  scaling in (1), an  $O(2)$  change in dissipation rate is entirely acceptable. Therefore, the Craig-Banner model is potentially useful for estimating the surface dissipation rate when the bulk epsilon and KEF are known, and for reasonable estimates of  $z_o$ . Figure 11 shows the dissipation rate can vary at least 2 orders of magnitude over the top 50 cm. Yet, it is the dissipation rate at the surface, and not the bulk measurement, that is crucial for estimates of air-sea gas transfer. Further study is required to refine this approach, with observations of dissipation rate profiles and  $z_o$  for different KEF rates due to rain. While the exact processes that set  $z_o$  are not known, stratification, drop size distribution, terminal and nonterminal drop velocities will all play a role. The success of modeling the dissipation profile during rainfall has implica-

tions for improved regional and global model predictions of gas transfer rates and eventually of trace gas budgets.

## 5. Conclusions

[64] The results of the Bio2 RainX III experiment show that near-surface turbulence is the dominant controlling factor for the enhancement of the of gas exchange rate in the ocean surface, even though the turbulent dissipation rate is strongly influenced by near-surface stratification. We observed a correlation of  $k_H(600)$  with increasing rain rate for the range of values investigated. The SF<sub>6</sub> evasion and ACFT results showing an increase in transfer velocity due to rain is consistent with physical measurements made during RainX III. Moreover, the high-resolution transfer rate and turbulence results presented here clearly show the causal relationship between rainfall, turbulence, stratification, and air-sea gas exchange. Here, profiles of the turbulent kinetic energy dissipation rate under rainfall were measured for the first time during a gas exchange experiment. Stratification modifies and leads to the trapping of  $\varepsilon$  near the surface. This not only has a profound effect on the enhanced  $k_H(600)$ , but also will play a role in diminishing the vertical mixing of mass transported to the air-water interface that is important as the driving potential in the flux of gas.

[65] The results clearly show that gas transfer scales with  $\varepsilon^{1/4}$  for a variety of different rain rates that include both the RainX II and RainX III data in Biosphere 2 for this system that is dominated by rain and includes effects of waves and artificial background turbulence (i.e., circulation pumps). While KEF may be relevant to measure the turbulent input to the system during rain events,  $\varepsilon$  is the most relevant response to all the modifications and transformations to the turbulent state that follow. The Craig-Banner turbulence model, modified for rain-induced turbulence instead of breaking wave turbulence, bears this out and successfully predicts the near-surface dissipation profile at the onset of the rain event before stratification plays a dominant role. This result has a profound impact on prediction and modeling gas transfer since it suggests that knowledge of the bulk turbulence and the forcing will result in the correct surface value of  $\varepsilon$  that is important to gas transfer and that is typically  $O(100)$  greater at the surface than in the bulk at a meter depth. Profiles of  $\varepsilon$  are therefore required to improve our estimates of  $\varepsilon$  at the surface and gain a further understanding of the interplay between rain, currents, wind, and waves and the transition between various forcing regimes.

[66] Although much has been learned about the influence of rain on air-water gas exchange, most studies have focused on laboratory or controlled experiments. It is clear that future gas exchange experiments considering rain forcing need to be performed in the natural environment. On the basis of the studies presented here, we argue that more research is needed to gauge the interaction of rain with wind [*Ho et al.*, 2007], stratification, waves [*Zappa et al.*, 2008], and other processes on gas exchange from the open ocean to wetlands. Not until the mechanisms behind rain-induced gas exchange have been sufficiently understood and the process been documented in nature can the ecosystem and global implications be evaluated. On an ecosystem scale, this would elucidate the impact of rain-induced gas exchange in quiescent environments such

as wetlands when performing nutrient studies or determining volatile pollutant transport. This also would meet the growing need among scientists to enhance our ability to determine the relative importance of the rain-induced fluxes of CO<sub>2</sub> and other trace gases in regional and global biogeochemical cycles.

[67] **Acknowledgments.** We thank S. Bissell, R. Cota, M. Hendricks, K. Mull, B. Shank, and A. Wright for their invaluable assistance during the experiment, F. Tubiana and D. Lebel for help with data processing and analysis, A. Jessup of the University of Washington's Applied Physics Laboratory for loaning their infrared imager and CO<sub>2</sub> laser, and B. Asher for his thoughtful and insightful discussions on bubbles and bubble-mediated effects. This work was funded by a generous grant from the David and Lucile Packard Foundation and the Lamont-Doherty Earth Observatory Climate Center. Additional funding was provided by the National Science Foundation (OCE-05-26677) and the Office of Naval Research Young Investigator Program (N00014-04-1-0621). This is LDEO contribution 7249.

## References

- Agrawal, Y. C., E. A. Terray, M. A. Donelan, P. A. Hwang, A. J. Williams III, W. M. Drennan, K. K. Kahma, and S. A. Kitaigorodskii (1992), Enhanced dissipation of kinetic energy beneath surface waves, *Nature*, **359**(6392), 219–220, doi:10.1038/359219a0.
- Anis, A., and J. N. Moum (1995), Surface wave-turbulence interactions: Scaling  $\epsilon(z)$  near the sea surface, *J. Phys. Oceanogr.*, **25**(9), 2025–2045, doi:10.1175/1520-0485(1995)025<2025:SWISNT>2.0.CO;2.
- Asher, W. E., and J. F. Pankow (1986), The interaction of mechanically generated turbulence and interfacial films with a liquid phase controlled gas/liquid transport process, *Tellus, Ser. B*, **38**(5), 305–318.
- Asher, W., and R. Wanninkhof (1998), Transient tracers and air-sea gas transfer, *J. Geophys. Res.*, **103**(C8), 15,939–15,958, doi:10.1029/98JC00379.
- Asher, W. E., L. M. Karle, B. J. Higgins, P. J. Farley, E. C. Monahan, and I. S. Leifer (1996), The influence of bubble plumes on air-seawater gas transfer velocities, *J. Geophys. Res.*, **101**(C5), 12,027–12,041, doi:10.1029/96JC00121.
- Asher, W. E., L. M. Karle, and B. J. Higgins (1997), On the differences between bubble-mediated air-water gas transfer in freshwater and seawater, *J. Mar. Res.*, **55**, 813–845, doi:10.1357/0022240973224210.
- Asher, W. E., A. T. Jessup, and M. A. Atmane (2004), Oceanic application of the active controlled flux technique for measuring air-sea transfer velocities of heat and gases, *J. Geophys. Res.*, **109**, C08S12, doi:10.1029/2003JC001862.
- Atkinson, M. J., H. Barnett, H. Aceves, C. Langdon, S. J. Carpenter, T. McConnaughey, E. Hochberg, M. Smith, and B. D. V. Marino (1999), The Biosphere 2 coral reef biome, *Ecol. Eng.*, **13**(1–4), 147–171, doi:10.1016/S0925-8574(98)00096-2.
- Atmane, M. A., W. E. Asher, and A. T. Jessup (2004), On the use of the active infrared technique to infer heat and gas transfer velocities at the air-water free surface, *J. Geophys. Res.*, **109**, C08S14, doi:10.1029/2003JC001805.
- Banerjee, S., D. S. Scott, and E. Rhodes (1968), Mass transfer to falling wavy liquid films in turbulent flow, *Ind. Eng. Chem. Fundam.*, **7**(1), 22–27, doi:10.1021/i160025a004.
- Batchelor, G. K. (1959), Small-scale variation of convected quantities like temperature in turbulent fluid. Part I. General discussion and the case of small conductivity, *J. Fluid Mech.*, **5**, 113–133, doi:10.1017/S002211205900009X.
- Bock, E. J., T. Hara, N. M. Frew, and W. R. McGillis (1999), Relationship between air-sea gas transfer and short wind waves, *J. Geophys. Res.*, **104**(C11), 25,821–25,831, doi:10.1029/1999JC900200.
- Brumley, B. H., and G. H. Jirka (1988), Air-water transfer of slightly soluble gases: Turbulence, interfacial processes and conceptual models, *PhysicoChem. Hydrodyn.*, **10**(3), 295–319.
- Clark, J. F., R. Wanninkhof, P. Schlosser, and H. J. Simpson (1994), Gas exchange rates in the tidal Hudson River using a dual tracer technique, *Tellus, Ser. B*, **46**(4), 274–285.
- Craeye, C., and P. Schlüssel (1998), Rainfall on the sea: Surface renewals and wave damping, *Boundary Layer Meteorol.*, **89**, 349–355, doi:10.1023/A:1001796911059.
- Craig, P. D., and M. L. Banner (1994), Modeling wave-enhanced turbulence in the ocean surface layer, *J. Phys. Oceanogr.*, **24**, 2546–2559, doi:10.1175/1520-0485(1994)024<2546:MWETIT>2.0.CO;2.
- Danckwerts, P. V. (1951), Significance of liquid-film coefficients in gas absorption, *Ind. Eng. Chem.*, **43**(6), 1460–1467, doi:10.1021/ie50498a055.
- Dickey, T. D., B. Hartman, D. Hammond, and E. Hurst (1984), A laboratory technique for investigating the relationship between gas transfer and fluid turbulence, in *Gas Transfer at Water Surfaces*, edited by W. Brutsaert and G. H. Jirka, pp. 93–100, D. Reidel, Norwell, Mass.
- Donlon, C. J., and I. S. Robinson (1997), Observations of the oceanic thermal skin in the Atlantic Ocean, *J. Geophys. Res.*, **102**(C8), 18,585–18,606, doi:10.1029/97JC00468.
- Downing, H. D., and D. Williams (1975), Optical constants of water in the infrared, *J. Geophys. Res.*, **80**(12), 1656–1661, doi:10.1029/JC080i012p01656.
- Farmer, D. M., C. L. McNeil, and B. D. Johnson (1993), Evidence for the importance of bubbles in increasing air-sea gas flux, *Nature*, **361**(6413), 620–623, doi:10.1038/361620a0.
- Frew, N. M. (1997), The role of organic films in air-sea gas exchange, in *The Sea Surface and Global Change*, edited by P. S. Liss and R. A. Duce, pp. 121–172, Cambridge Univ. Press, Cambridge, U. K.
- Frew, N. M., et al. (2004), Air-sea gas transfer: Its dependence on wind stress, small-scale roughness, and surface films, *J. Geophys. Res.*, **109**, C08S17, doi:10.1029/2003JC002131.
- Gemmrich, J. R., and D. M. Farmer (1999), Near-surface turbulence and thermal structure in a wind-driven sea, *J. Phys. Oceanogr.*, **29**, 480–499, doi:10.1175/1520-0485(1999)029<0480:NSTATS>2.0.CO;2.
- Gemmrich, J. R., and D. M. Farmer (2004), Near-surface turbulence in the presence of breaking waves, *J. Phys. Oceanogr.*, **34**, 1067–1086, doi:10.1175/1520-0485(2004)034<1067:NTITPO>2.0.CO;2.
- Green, T., and D. F. Houk (1979), The mixing of rain with near-surface water, *J. Fluid Mech.*, **90**(3), 569–588, doi:10.1017/S0022112079002408.
- Harriott, P. (1962), A random eddy modification of the penetration theory, *Chem. Eng. Sci.*, **17**, 149–154, doi:10.1016/0009-2509(62)80026-8.
- Haußecker, H., S. Reinelt, and B. Jähne (1995), Heat as a proxy tracer for gas exchange measurements in the field: Principles and technical realization, in *Air-Water Gas Transfer*, edited by B. Jähne and E. C. Monahan, pp. 405–413, AEON, Hanau, Germany.
- Hill, R. H. (1972), Laboratory measurement of heat transfer and thermal structure near an air-water interface, *J. Phys. Oceanogr.*, **2**, 190–198, doi:10.1175/1520-0485(1972)002<0190:LMOHTA>2.0.CO;2.
- Ho, D. T., L. F. Bliven, R. Wanninkhof, and P. Schlosser (1997), The effect of rain on air-water gas exchange, *Tellus, Ser. B*, **49**(2), 149–158.
- Ho, D. T., W. E. Asher, L. F. Bliven, P. Schlosser, and E. L. Gordan (2000), On the mechanisms of rain-induced air-water gas exchange, *J. Geophys. Res.*, **105**(C10), 24,045–24,057, doi:10.1029/1999JC000280.
- Ho, D. T., C. J. Zappa, W. R. McGillis, L. F. Bliven, B. Ward, J. W. H. Dacey, P. Schlosser, and M. B. Hendricks (2004), Influence of rain on air-sea gas exchange: Lessons from a model ocean, *J. Geophys. Res.*, **109**, C08S18, doi:10.1029/2003JC001806.
- Ho, D. T., C. S. Law, M. J. Smith, P. Schlosser, M. Harvey, and P. Hill (2006), Measurements of air-sea gas exchange at high wind speeds in the Southern Ocean: Implications for global parameterizations, *Geophys. Res. Lett.*, **33**, L16611, doi:10.1029/2006GL026817.
- Ho, D. T., F. Veron, E. Harrison, L. F. Bliven, N. Scott, and W. R. McGillis (2007), The combined effect of rain and wind on air-water gas exchange: A feasibility study, *J. Mar. Syst.*, **66**, 150–160, doi:10.1016/j.jmarsys.2006.02.012.
- Jähne, B., K. O. Munnich, R. Bosinger, A. Dutzi, W. Huber, and P. Libner (1987), On the parameters influencing air-water gas exchange, *J. Geophys. Res.*, **92**(C2), 1937–1949, doi:10.1029/JC092iC02p01937.
- Jähne, B., P. Libner, R. Fischer, T. Billen, and E. J. Plate (1989), Investigating the transfer processes across the free aqueous viscous boundary layer by the controlled flux method, *Tellus, Ser. B*, **41**(2), 177–195.
- Jessup, A. T., C. J. Zappa, and H. Yeh (1997), Defining and quantifying microscale wave breaking with infrared imagery, *J. Geophys. Res.*, **102**(C10), 23,145–23,154, doi:10.1029/97JC01449.
- Katsaros, K. B. (1980), The aqueous thermal boundary layer, *Boundary Layer Meteorol.*, **18**, 107–127, doi:10.1007/BF00117914.
- Keeling, R. F. (1993), On the role of large bubbles in air-sea gas exchange and supersaturation in the ocean, *J. Mar. Res.*, **51**, 237–271, doi:10.1357/0022240933223800.
- Kitaigorodskii, S. A. (1984), On the fluid dynamical theory of turbulent gas transfer across an air-sea interface in the presence of breaking wind-waves, *J. Phys. Oceanogr.*, **14**(5), 960–972, doi:10.1175/1520-0485(1984)014<0960:OTFDTO>2.0.CO;2.
- Lamont, J. C., and D. S. Scott (1970), An eddy cell model of mass transfer into the surface of a turbulent liquid, *AIChE J.*, **16**, 512–519.
- Lange, P. A., G. V. D. Graaf, and M. Gade (2000), Rain-induced subsurface turbulence measured using image processing methods, *Proc. IGARSS*, **7**, 3175–3177.
- Ledwell, J. J. (1984), The variation of the gas transfer coefficient with molecular diffusivity, in *Gas Transfer at Water Surfaces*, edited by W. Brutsaert and G. H. Jirka, pp. 293–302, D. Reidel, Norwell, Mass.

- Lhermitte, R. M. (1988), Observation of rain at vertical incidence with a 94 GHz Doppler radar: An insight on Mie scattering, *Geophys. Res. Lett.*, *15*(10), 1125–1128, doi:10.1029/GL015i010p01125.
- Liss, P. S., and L. Merlivat (1986), Air-sea gas exchange rates: Introduction and synthesis, in *The Role of Air-Sea Exchange in Geochemical Cycling*, edited by P. Buat-Ménard, pp. 113–127, D. Reidel, Norwell, Mass.
- Liss, P. S., and P. G. Slater (1974), Flux of gases across the air-sea interface, *Nature*, *247*(5438), 181–184, doi:10.1038/247181a0.
- Lorke, A., and F. Peeters (2006), Toward a unified scaling relation for interfacial fluxes, *J. Phys. Oceanogr.*, *36*, 955–961, doi:10.1175/JPO2903.1.
- Lumley, J. L., and E. A. Terray (1983), Kinematics of turbulence converted by a random wave field, *J. Phys. Oceanogr.*, *13*, 2000–2007, doi:10.1175/1520-0485(1983)013<2000:KOTCBA>2.0.CO;2.
- Ma, B. B., and J. A. Nystuen (2005), Passive acoustic detection and measurement of rainfall at sea, *J. Atmos. Oceanic Technol.*, *22*(8), 1225–1248, doi:10.1175/JTECH1773.1.
- Marshall, J. S., and W. M. Palmer (1948), The distribution of the raindrops with size, *J. Meteorol.*, *5*, 165–166.
- McAlister, E. D., and W. McLeish (1969), Heat transfer in the top millimeter of the ocean, *J. Geophys. Res.*, *74*(13), 3408–3414, doi:10.1029/JC074i013p03408.
- McAlister, E. D., and W. McLeish (1970), A radiometric system for airborne measurement of the total heat flow from the sea, *Appl. Opt.*, *9*(12), 2697–2705, doi:10.1364/AO.9.002697.
- Mellor, G. L., and T. Yamada (1982), Development of a turbulence closure model for geophysical problems, *Rev. Geophys. Space Phys.*, *20*(4), 851–875, doi:10.1029/RG020i004p00851.
- Melville, W. K. (1996), The role of surface-wave breaking in air-sea interaction, *Annu. Rev. Fluid Mech.*, *28*, 279–321, doi:10.1146/annurev.fl.28.010196.001431.
- Merlivat, L., and L. Memery (1983), Gas Exchange Across an Air-Water Interface: Experimental Results and Modeling of Bubble Contribution to Transfer, *J. Geophys. Res.*, *88*(C1), 707–724, doi:10.1029/JC088iC01p00707.
- Nightingale, P. D., G. Malin, C. S. Law, A. J. Watson, P. S. Liss, M. I. Liddicoat, J. Boutin, and R. C. Upstill-Goddard (2000), In situ evaluation of air-sea gas exchange parameterizations using novel conservative and volatile tracers, *Global Biogeochem. Cycles*, *14*(1), 373–387, doi:10.1029/1999GB900091.
- Nystuen, J. A. (2001), Listening to raindrops from underwater: An acoustic disdrometer, *J. Atmos. Oceanic Technol.*, *18*(10), 1640–1657, doi:10.1175/1520-0426(2001)018<1640:LTRFUA>2.0.CO;2.
- Olsen, R. L., D. V. Rogers, and D. B. Hodge (1978), Arb relation in calculation of rain attenuation, *IEEE Trans. Antennas Propag.*, *26*(2), 318–329, doi:10.1109/TAP.1978.1141845.
- Robinson, I. S., N. C. Wells, and H. Charnock (1984), The sea surface thermal boundary layer and its relevance to the measurement of sea surface temperature by airborne and spaceborne radiometers, *Int. J. Remote Sens.*, *5*(1), 19–45, doi:10.1080/01431168408948787.
- Schlüssel, P., W. J. Emery, H. Grassl, and T. Mammen (1990), On the bulk-skin temperature difference and its impact on satellite remote sensing of sea surface temperature, *J. Geophys. Res.*, *95*(C8), 13,341–13,356, doi:10.1029/JC095iC08p13341.
- Schlüssel, P., A. V. Soloviev, and W. J. Emery (1997), Cool and freshwater skin of the ocean during rainfall, *Boundary Layer Meteorol.*, *82*, 437–472, doi:10.1023/A:1000225700380.
- Scott, J. C. (1975), The role of salt in whitecap persistence, *Deep Sea Res.*, *22*, 653–657.
- Takagaki, N., and S. Komori (2007), Effects of rainfall on mass transfer across the air-water interface, *J. Geophys. Res.*, *112*, C06006, doi:10.1029/2006JC003752.
- Terray, E. A., M. A. Donelan, Y. C. Agrawal, W. M. Drennan, K. K. Kahma, I. A. J. Williams, P. A. Hwang, and S. A. Kitaigorodskii (1996), Estimates of kinetic energy dissipation under surface waves, *J. Phys. Oceanogr.*, *26*(5), 792–807, doi:10.1175/1520-0485(1996)026<0792:EOKEDU>2.0.CO;2.
- Veron, F., and W. K. Melville (1999), Pulse-to-pulse coherent Doppler measurements of waves and turbulence, *J. Atmos. Oceanic Technol.*, *16*(11), 1580–1597, doi:10.1175/1520-0426(1999)016<1580:PTPCDM>2.0.CO;2.
- Wanninkhof, R. (1992), Relationship between wind speed and gas exchange over the ocean, *J. Geophys. Res.*, *97*(C5), 7373–7382, doi:10.1029/92JC00188.
- Wanninkhof, R., and W. R. McGillis (1999), A cubic relationship between air-sea CO<sub>2</sub> exchange and wind speed, *Geophys. Res. Lett.*, *26*(13), 1889–1892, doi:10.1029/1999GL900363.
- Wick, G. A., W. J. Emery, L. H. Kantha, and P. Schlüssel (1996), The behavior of the bulk-skin sea surface temperature difference under varying wind speed and heat flux, *J. Phys. Oceanogr.*, *26*(10), 1969–1988, doi:10.1175/1520-0485(1996)026<1969:TBOTBS>2.0.CO;2.
- Woolf, D. K. (1993), Bubbles and the air-sea transfer velocity of gases, *Atmos. Ocean*, *31*, 517–540.
- Woolf, D. K., and S. A. Thorpe (1991), Bubbles and the air-sea exchange of gases in near saturation conditions, *J. Mar. Res.*, *49*, 435–466, doi:10.1357/002224091784995765.
- Wu, J. (1971), An estimation of oceanic thermal-sublayer thickness, *J. Phys. Oceanogr.*, *1*, 284–286, doi:10.1175/1520-0485(1971)001<0284:AEOOTS>2.0.CO;2.
- Zappa, C. J., A. T. Jessup, and H. H. Yeh (1998), Skin-layer recovery of free-surface wakes: Relationship to surface renewal and dependence on heat flux and background turbulence, *J. Geophys. Res.*, *103*(C10), 21,711–21,722, doi:10.1029/98JC01942.
- Zappa, C. J., W. E. Asher, and A. T. Jessup (2001), Microscale wave breaking and air-water gas transfer, *J. Geophys. Res.*, *106*(C5), 9385–9391, doi:10.1029/2000JC000262.
- Zappa, C. J., P. A. Raymond, E. Terray, and W. R. McGillis (2003), Variation in surface turbulence and the gas transfer velocity over a tidal cycle in a macro-tidal estuary, *Estuaries*, *26*(6), 1401–1415, doi:10.1007/BF02803649.
- Zappa, C. J., W. E. Asher, A. T. Jessup, J. Klinke, and S. R. Long (2004), Microbreaking and the enhancement of air-water transfer velocity, *J. Geophys. Res.*, *109*, C08S16, doi:10.1029/2003JC001897.
- Zappa, C. J., W. R. McGillis, P. A. Raymond, J. B. Edson, E. J. Hints, H. J. Zemmleink, J. W. H. Dacey, and D. T. Ho (2007), Environmental turbulent mixing controls on air-water gas exchange in marine and aquatic systems, *Geophys. Res. Lett.*, *34*, L10601, doi:10.1029/2006GL028790.
- Zappa, C. J., M. L. Banner, H. Schultz, A. Corrada-Emmanuel, L. B. Wolff, and J. Yalcin (2008), Retrieval of short ocean wave slope using polarimetric imaging, *Meas. Sci. Technol.*, *19*(055503), doi:10.1088/0957-0233/19/10/055503.
- Zedel, L., A. E. Hay, R. Cabrera, and A. Lohmann (1996), Performance of a single-beam pulse-to-pulse coherent Doppler profiler, *IEEE J. Oceanic Eng.*, *21*(3), 290–297, doi:10.1109/48.508159.

M. L. Banner, W. R. McGillis, and C. J. Zappa, Lamont-Doherty Earth Observatory, Earth Institute at Columbia University, Palisades, NY 10964, USA. (zappa@ldeo.columbia.edu)

L. F. Bliven, Laboratory for Hydrospheric Processes, NASA Goddard Space Flight Center, Wallops Island, VA 23337, USA.

J. W. H. Dacey, Biology Department, Woods Hole Oceanographic Institution, Woods Hole, MA 02543, USA.

D. T. Ho, Department of Oceanography, University of Hawai'i at Manoa, Honolulu, HI 96822, USA.

B. Ma, Electrical and Computer Engineering, Portland State University, Portland, OR 97207, USA.

J. Nystuen, Applied Physics Laboratory, University of Washington, Seattle, WA 98105, USA.